CALIBRATION OF THE MU2E ABSOLUTE MOMENTUM SCALE USING $\pi^+ \to e^+\nu_e$

by

Xiaobing Shi

A Dissertation

Submitted to the Faculty of Purdue University

In Partial Fulfillment of the Requirements for the degree of

Doctor of Philosophy

Department of Physics and Astronomy

West Lafayette, Indiana

May 2024

THE PURDUE UNIVERSITY GRADUATE SCHOOL
STATEMENT OF COMMITTEE APPROVAL

Dr. David Koltick, Chair

Department of Physics and Astronomy

Dr. Francis Robicheaux

Department of Physics and Astronomy

Dr. Martin Kruczenski

Department of Physics and Astronomy

Dr. Gabor Csathy

Department of Physics and Astronomy

Approved by:

Dr. Gabor Csathy, Head, Department of Physics and Astronomy

ACKNOWLEDGMENTS

First, I would like to thank my former PhD advisor Professor John Finley, for starting me in the Mu2e experiment and his excellent guidance during my study over the last five years. I would also like to thank Professor David Koltick for taking over the role of advisor after the passing of Professor Finley and helping me wrapping up the PhD thesis. I am also indebted to Dr. Michael Hedges for his technical expertise and advice for the project. My thanks go out to many people who provided useful advices and whom I had fruitful discussions with, including Dr. Robert Bernstein, Dr. Pavel Murat, Dr. James Mott, Dr. James Miller, and Dr. Stefano Di Falco at the Mu2e collaboration. I am grateful to the love from my parents, and the supports from friends and colleagues throughout my life as a graduate student in Purdue. Last but not least, I would like to thank Dr. Kruczenski, Dr. Robicheaux and Dr. Csathy for attending my thesis defense and reviewing the draft of thesis.

TABLE OF CONTENTS

LIST OF TABLES

LIST OF FIGURES

ABSTRACT

The Mu2e experiment will search for neutrinoless, coherent conversion of a muon into an electron in the field of an aluminum nucleus ($\mu^- N \rightarrow e^- N$) at the sensitivity level of 10^{-17}. This conversion process is an example of Charged Lepton Flavor Violation (CLFV), which has never been observed experimentally before. The Mu2e experiment tracker is designed to accurately detect the 105 MeV/c conversion electron (CE) momentum in a uniform 1 T magnetic field. The mono-energetic positrons (e^+) at 69.8 MeV from the decay of positively-charged pions (π^+) that have stopped in the aluminum stopping target are investigated as a calibration source to measure the accuracy of absolute momentum scale. The backgrounds for the calibration arise from μ^+ decay-in-flight (DIF) backgrounds and other stopped π^+ decays that produce reconstructed e^+ tracks mimicking a signal trajectory originating from the stopping target. The most significant background is the μ-DIF background. Therefore, we identified the need for a *momentum degrader* placed at the entry of the Detector Solenoid, to increase the pion stops in the stopping target and suppress the μ-DIF background. The material of the degrader is chosen to be titanium (Ti). The thickness of degrader is optimized by the pion stops efficiency to muon flux efficiency ratio and the 4mm Ti degrader is the optimized one. The calibration signal and backgrounds are simulated with the 3mm and 4mm Ti degrader. The ratio of S/B is used as a figure of merit, S/B $\sim$ 1.85 for the 3mm Ti degrader and S/B $\sim$ 2.93 for the 4mm Ti degrader. The 4mm Ti degrader performs better than the 3mm Ti degrader in terms of S/B ratio. By fitting the reconstructed momentum spectra of signal and backgrounds, we extract the signal distribution peak and width of $x_0 = 69.268 \pm 0.013$ MeV/c and $\sigma = 0.324 \pm 0.009$ MeV/c (with the 3mm Ti degrader), $x_0 = 69.263 \pm 0.013$ MeV/c and $\sigma = 0.299 \pm 0.009$ MeV/c (with the 4mm Ti degrader). We also show that the peak shifts by backgrounds for both degraders are within 100 keV/c momentum scale accuracy requirement.

1. OVERVIEW

The Mu2e Experiment[1] at Fermi National Accelerator Laboratory (Fermilab) will search for the Charged Lepton Flavor Violation (CLFV) process of coherent muon-to-electron conversion $\mu^- N \rightarrow e^- N$ on an aluminum target. Detecting the resulting $\sim$ 105 MeV/c conversion electron (CE) signal requires excellent momentum resolution in the presence of muon decay-in-orbit (DIO) background events, as shown in Figure 1.1. The Mu2e Experiment has estimated that it must achieve a momentum resolution of order 100 keV/c at the CE momentum scale to achieve its stated goals of 10^4 improvement over the existing experimental bounds for this process in several years of running[1], [2].

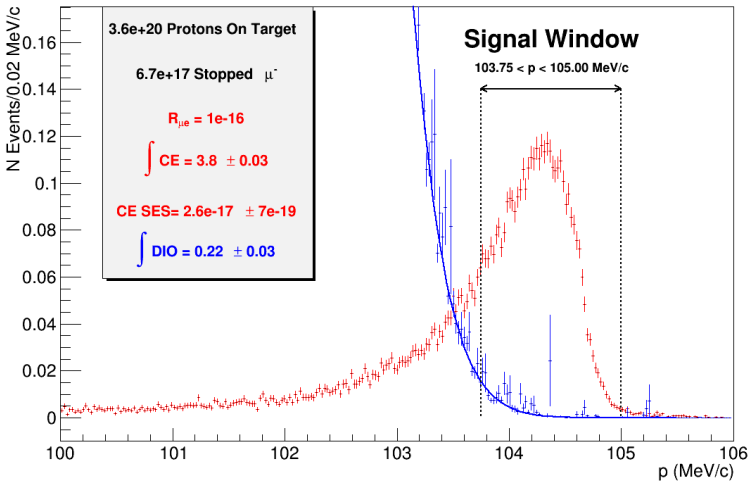

Figure 1.1. The reconstructed momenta spectrum for DIO background (Blue) and conversion electron (CE) signal (Red) surviving the track selection criteria, assuming $R_{\mu e} = 1 \times 10^{-16}$. The two vertical dashed lines indicate the momentum search window, 103.75 < P < 105.00 MeV/c. Adapted from Ref. [1].

Assuring that this resolution requirement is met necessitates a calibration procedure for the Mu2e experiment. We have identified and investigated using 70 MeV/c positrons (e^+) from the decays of positively-charged pions (π^+) that have stopped in the aluminum stopping target as a calibration source to measure the absolute momentum scale and momentum resolution.

The Mu2e experiment is designed to stop negatively-charged muons μ^- and detect their decay products. While the stopped π^- would also produce the same signal, nuclear effects such as Radiative Pion Capture (RPC) would convolve the desired calibration signal. Fortunately, Mu2e is designed in such a way that changes can be made to run with a positive particle beam instead of a negative particle beam by rotating a central collimator in the transport section of the beamline. The magnetic field in this region is designed to separate positive and negative particles in the vertical plane, and the rotatable collimator can be configured to allow acceptance of one region while blocking the other. The Detector Solenoid (DS) magnetic field must also be reduced by the ratio of the momenta of the calibration signal to the CE signal, or about 70% in order to increase acceptance to the 70 MeV/c calibration signal. To further maximize the signal originating from stopped π^+, we have identified the need for a *momentum degrader* placed upstream of the stopping target. The degrader is necessary because the minimal mass of the stopping target is ideal for stopping μ, while the π momentum spectrum is much higher, resulting in most of the π-beam passing straight through the target if their momenta is not reduced beforehand. Furthermore, the degrader also significantly reduces the incoming μ momentum spectrum, consequently reducing the impact of μ decay-in-flight backgrounds. The degrader is therefore essential to bring the total signal-to-background ratio to an acceptable level for this calibration mode. The material of the degrader is chosen to be titanium (Ti).

The backgrounds for the calibration arise from beam-backgrounds and stopped π^+ decays that produce reconstructed e^+ tracks mimicking a signal trajectory originating from the stopping target:

- The beam-backgrounds originate from beam particles such as μ^+ as well as π^+ that enter the DS and produce decay particles in flight that are then reconstructed.
- Stopped $\pi^+ \to e^+$ in degrader
- Stopped $\pi^+ \to \mu^+$ in stopping target and degrader

The most significant background is the aforementioned $\mu^+ \to e^+\nu\nu$ decay-in-flight where the e^+ track is reconstructed in the Mu2e detectors with a momentum at or near the expected

70 MeV/c calibration signal. Therefore, the Ti degrader thickness is optimized by the pion stops efficiency to muon flux efficiency ratio. The pion stops efficiency is defined as the number of pion stops in the stopping target per proton-on-target, and the muon flux efficiency is defined as the number of muons with momentum larger than 30 MeV/c entering the DS per proton-on-target. Figure 1.2 shows the pion stops efficiency to muon flux efficiency ratio as a function of degrader thickness. The 4mm Ti degrader is the optimized one that makes the largest signal-to-background ratio.

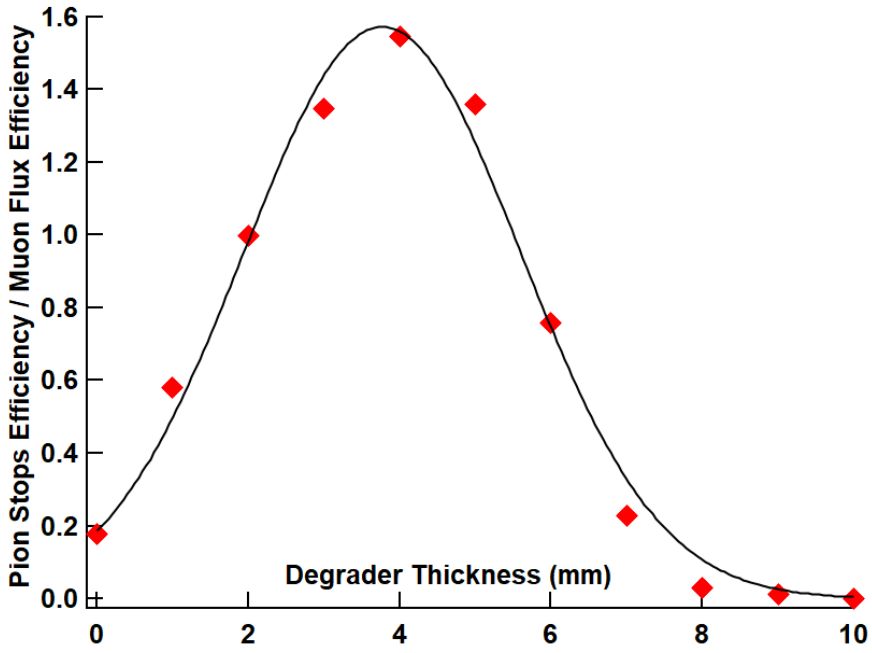

Figure 1.2. The pion stops efficiency to muon flux efficiency ratio as a function of degrader thickness.The black curve is given by Gaussian fitting.

Using the Mu2e Offline simulation framework based on Geant4[3]–[5], the expected signal and background processes and the Mu2e event reconstruction are simulated with the 3mm and 4mm Ti degrader at the level of $O(10^{13}) - O(10^{15})$ protons-on-target (POT). The resulting reconstructed momentum distributions of signal and backgrounds are presented in Figure 1.3. All the reconstructed tracks are required to pass the pre-selection cuts and T_0 (reconstructed time of track) cut between 300-400 ns. From these distributions, the signal and background yields between 67.5-70.0 MeV/c are calculated, as shown in Table 1.1.

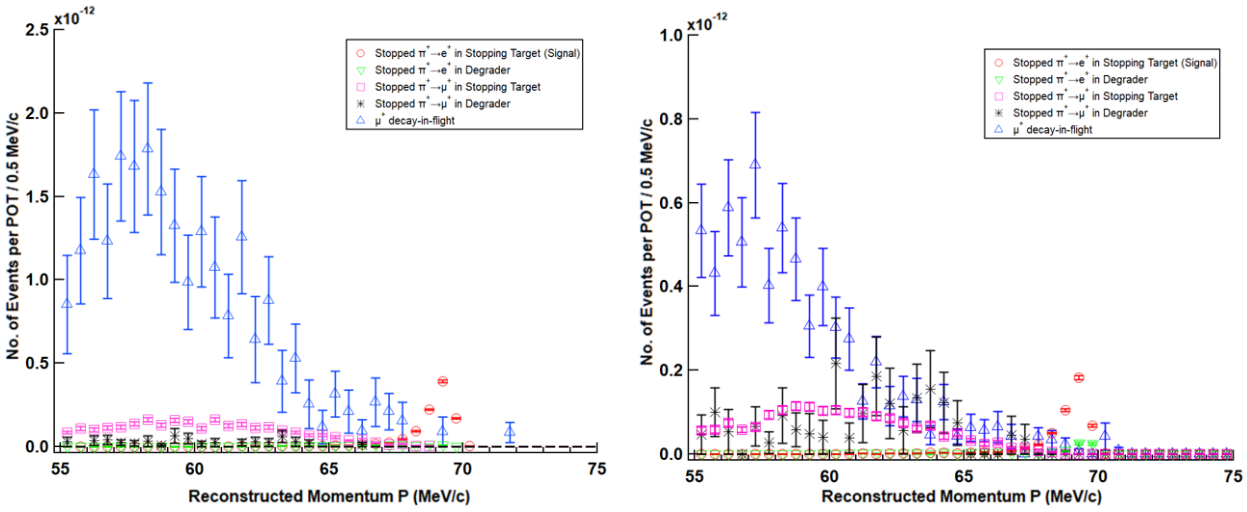

(a) (b)

Figure 1.3. Resulting momentum distribution of the stopped-π calibration signal on top of expected backgrounds.(a) 3mm Ti degrader. (b) 4mm Ti degrader. All the reconstructed tracks are required to pass the pre-selection cuts and T_0 (reconstructed time of track) cut between 300-400 ns.

Table 1.1. Summary of the signal and background yields, normalized to protons-on-target (POT). The measurement uncertainties are statistical.

	Yield (3mm)	Yield (4mm)
Signal	$(9.21 \pm 0.11) \times 10^{-13}$	$(4.43 \pm 0.07) \times 10^{-13}$
Total Background	$(4.99 \pm 0.77) \times 10^{-13}$	$(1.51 \pm 0.16) \times 10^{-13}$
S/B	1.85	2.93

From the Monte Carlo simulation, we have known shape functions, F_s and F_b for signal and background. We also have an observed shape function, F_o. The shape functions F_s, F_b and F_o can be normalized, so that,

$$(S+B)F_o = S \cdot F_s + B \cdot F_b \tag{1.1}$$

where S(T) and B(T) are signal and background yields as functions of degrader thickness T. To maximize the knowledge of F_s, S/B should be maximized,

$$(1 + S/B)F_o = (S/B)F_s + F_b \tag{1.2}$$

Therefore, S/B is used as a figure of merit, as $B \gg 0$. The 4mm Ti degrader performs better than the 3mm Ti degrader in terms of the S/B ratio.

By fitting the reconstructed momentum distributions of signal (in Figure 1.3) using the crystal ball function, we extract the signal distribution peak and width of $x_0 = 69.268 \pm 0.013$ MeV/c and $\sigma = 0.324 \pm 0.009$ MeV/c (with the 3mm Ti degrader), $x_0 = 69.263 \pm 0.013$ MeV/c and $\sigma = 0.299 \pm 0.009$ MeV/c (with the 4mm Ti degrader). The peak shifts caused by backgrounds are summarized in Table 1.2.

Table 1.2. Summary of the peak shifts caused by backgrounds. The uncertainties are statistical.

Background	3mm	4mm
$\pi^+ \to e^+$ in Degrader	-9 ± 16 keV/c	$+88 \pm 21$ keV/c
$\pi^+ \to \mu^+$ in Stopping Target	$+2 \pm 20$ keV/c	-1 ± 19 keV/c
μ^+ Decay-In-Flight	-2 ± 34 keV/c	-7 ± 21 keV/c
Total	-9 ± 43 keV/c	$+80 \pm 35$ keV/c

The statistical uncertainties in Table 1.2 can be reduced to sub-keV level if we run the calibration with $O(10^{16})$ POT, which corresponds $\sim$ 1 week run with 1/50th of nominal intensity. Figure 1.4 shows the momentum spectra of reconstructed events with the 3mm (Black) and 4mm (Red) Ti degrader when running the calibration with 3×10^{16} POT. The peak shifts by backgrounds for both degraders are within 100 keV/c momentum scale accuracy requirement.

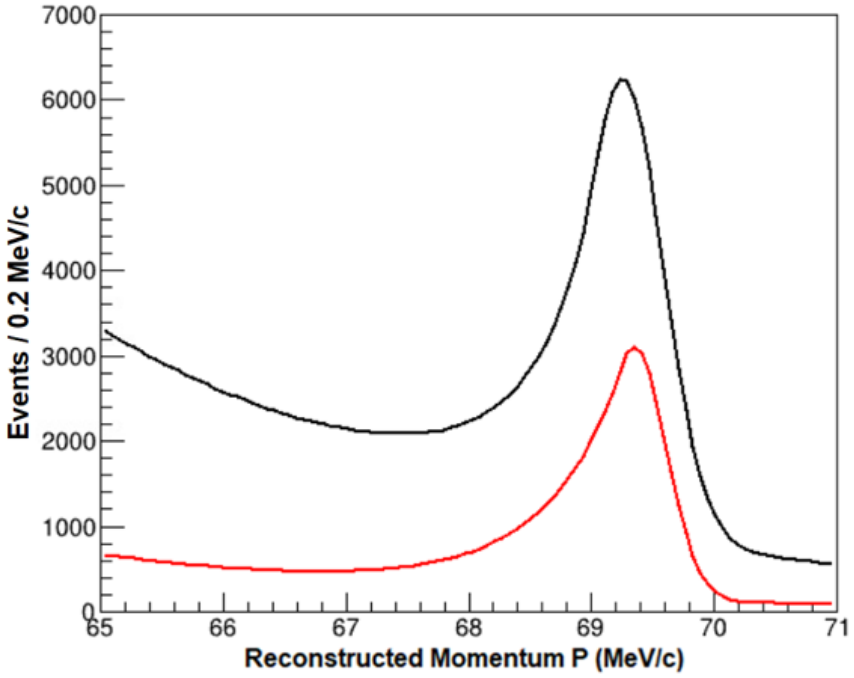

Figure 1.4. The momentum spectra of reconstructed events with the 3mm (Black) and 4mm (Red) Ti degrader when running the calibration with 3×10^{16} POT. There are 76394 reconstructed events for the 3mm Ti degrader, 24175 reconstructed events for the 4mm Ti degrader. All the reconstructed events are required to pass the pre-selection cuts and T_0 (reconstructed time of track) cut between 300-400 ns.

2. INTRODUCTION

During the latter half of the 20th century, the Standard Model of particle physics puts together the most successful framework to describe our universe on the fundamental level. However, the Standard Model is not a complete theory and leaves many questions unexplained. For instance, the Standard Model cannot provide any candidate for dark matter particle. The neutrino oscillation is a direct challenge to the lepton flavor numbers conservation in the Standard Model. Therefore, many Beyond Standard Model theories are developed [6], [7], and await the validation in high energy physics experiments.

2.1 Charged Lepton Flavor Violation

Charged Lepton Flavor Violation (CLFV) [8]–[12] is the violation of lepton flavor number among the charged leptons, which is forbidden in the Standard Model. In the minimal extension to the Standard Model [10], one of the CLFV process $\mu \to e\gamma$ can occur through loop diagrams (Figure 2.1)

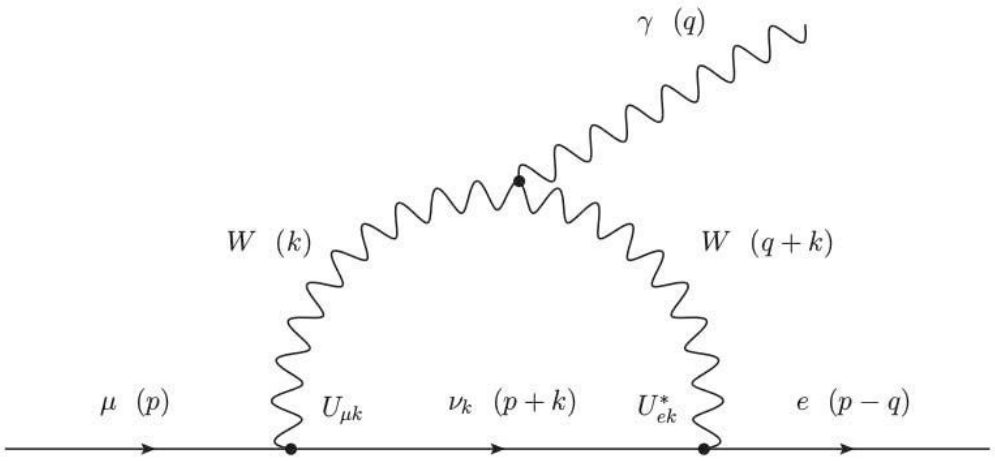

Figure 2.1. Diagram contributing to $\mu \to e\gamma$ in the SM with massive neutrinos. The four-momenta of the particles are indicated in parenthesis [13].

The branching ratio is

$$\mathrm{BR}(\mu \to e\gamma) = \frac{3\alpha}{32\pi}\left|\sum_{k=1,3}\frac{U_{\mu k}U^*_{ek}m^2_{\nu_k}}{M^2_W}\right|^2 \sim 10^{-54} \tag{2.1}$$

The huge mass difference between neutrino and W boson determines that the branch ratio to be $O(10^{-54})$, which is unmesurable small [13]. However, many well-motivated physics models predict rates for CLFV processes that are within a few orders of magnitude of the current experimental bounds. These include the MSSM with right-handed neutrinos, SUSY with R-parity violation as well as models with leptoquarks, new gauge bosons, large extra-dimensions, and a non-minimal Higgs sector [14].

The search for CLFV processes is based on the rare decays of muons, taus, kaons, and B mesons. Various CLFV processes have been searched in many experiments, and the current upper limits of branch ratio and the sensitivity of next generation experiments are listed in Table 2.1. As shown in Figure 2.2, the upper limits of branch ratio for muon rare decay channels have been improved quickly during past decades and reach the lowest branch ratio limits compared to other channels in Table 2.1. Because the small mass muon has less decay channels, then simpler backgrounds compared to heavier particles and the existence of intense muon sources. The experimental upper limits (all at 90% CL) on the branching ratios are: BR($\mu^+ \to e^+\gamma$) $< 4.2\times10^{-13}$ by MEG experiment [15], [16], BR($\mu^+ \to e^+e^+e^-$) $< 1.0 \times 10^{-12}$ by SINDRUM experiment [17], and $R_{\mu e}$(Au)(muon-to-electron conversion on gold)$< 7.0 \times 10^{-13}$ by SINDRUM II experiment [18]. For the next generation experiments of the muon sector, the MEG-II experiment for $\mu^+ \to e^+\gamma$ will be upgraded to an expected sensitivity of 6×10^{-14} [19]. The Mu3e experiment will search for the $\mu^+ \to e^+e^+e^-$ with a sensitivity of 10^{-16} [20], [21]. The Mu2e experiment at Fermilab [1], as well as the COMET experiment at J-PARC [22] aim to achieve sensitivities of 10^{-17} on $R_{\mu e}(Al)$, which improve the current upper limit by four orders of magnitude.

We can estimate the sensitivity of three muon rare decay channels in a model-independent way by adding two qualitatively different lepton flavor violation effective operators to the Standard Model Lagrangian [29]:

$$L_{CLFV} = \frac{m_\mu}{(1+\kappa)\,\Lambda^2}\bar{\mu}_R\sigma_{\mu\nu}e_L F^{\mu\nu} + \frac{\kappa}{(1+\kappa)\Lambda^2}\bar{\mu}_L\gamma_\mu e_L\left(\sum_{q=u,d}\bar{q}_L\gamma^u q_L\right) \tag{2.2}$$

Here Λ is the effective mass scale of New Physics; κ is a dimensionless parameter that controls the relative contribution of the two terms; L,R represent the chirality of Standard Model

Table 2.1. Branching ratio upper limits of CLFV processes (confidence level CL = 90%)

Process	Upper Limit	Next Generation Experiment
$\tau \to \mu\gamma$	$< 4.4 \times 10^{-8}$[23]	
$\tau \to e\gamma$	$< 3.3 \times 10^{-8}$[23]	10^{-9} to 10^{-10}
$\tau \to \mu\mu\mu$	$< 2.1 \times 10^{-8}$[24]	Belle II LHCb
$\tau \to eee$	$< 2.7 \times 10^{-8}$[24]	
$B^0 \to e\mu$	$< 2.8 \times 10^{-9}$[25]	Belle II LHCb
$B^+ \to K^+e^-\mu^+$	$< 6.4 \times 10^{-9}$[26]	
$K_L^0 \to e\mu$	$< 4.7 \times 10^{-12}$[27]	NA62
$K^+ \to \pi^+\mu^+e^-$	$< 1.3 \times 10^{-11}$[28]	
$\mu^+ \to e^+\gamma$	$< 4.2 \times 10^{-13}$[15]	10^{-14}(MEG-II)
$\mu^+ \to e^+e^+e^-$	$< 1.0 \times 10^{-12}$[17]	10^{-16}(Mu3e)
$\mu^-\text{Au} \to e^-\text{Au}$	$< 7.0 \times 10^{-13}$[18]	10^{-17}(Mu2e,COMET)

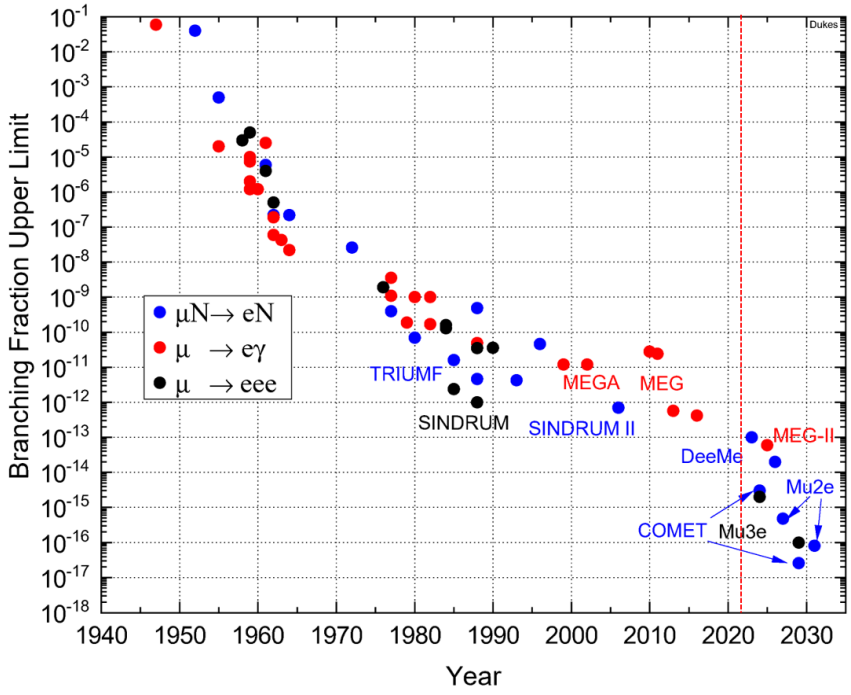

Figure 2.2. Limits of CLFV searches in the muon sector, $\mu^+ \to e^+\gamma$, $\mu^+ \to e^+e^+e^-$ and $\mu^-N \to e^-N$. The next generation $\mu^-N \to e^-N$ search, the Mu2e experiment in FNAL, will improve the current limit by four orders of magnitude, to achieve sensitivity at the order of 10^{-17}.

fermion fields; $F^{\mu\nu}$ is the photon field strength and m_μ is the muon mass. The first "loop" term is a flavor-changing magnetic moment operator, which mediates $\mu^+ \to e^+\gamma$ directly

and at order α for $\mu^+ \to e^+e^+e^-$ and $\mu^- N \to e^- N$, since the photon is real in $\mu^+ \to e^+\gamma$ and virtual in $\mu^+ \to e^+e^+e^-$ and $\mu^- N \to e^- N$; the second "contact" term is a four-fermion interaction operator, including contact terms and a variety of other processes not resulting in an on-mass-shell photon, which mediates at the leading order in $\mu^+ \to e^+e^+e^-$ and $\mu^- N \to e^- N$. Therefore, the $\mu^+ \to e^+e^+e^-$ and $\mu^- N \to e^- N$ processes are sensitive to New Physics regardless of the relative contributions of the "loop" and "contact" terms.

The results from two processes $\mu^+ \to e^+\gamma$ and $\mu^- N \to e^- N$ are complementary to each other in unravelling the underlying physics. Figure 2.3 shows the New Physics scale Λ probed by past and upcoming experiments as a function of κ. The colored regions of parameter space have been excluded by past experiments (red by the MEG experiment and blue by the SINDRUM-II experiment). The solid and dashed lines in the figure represent contours of different branching ratios. When $\kappa \ll 1$, the first term in Equation 2.1 is dominant, the mass scale Λ probed for $\mu^+ \to e^+\gamma$ at the level of 10^{-14} is comparable to that for $\mu^- N \to e^- N$ at the level of 10^{-16}. Thus if MEG-II observes a signal, then Mu2e should as well. When $\kappa \gg 1$, the second term dominates, experiments for $\mu^- N \to e^- N$ are more sensitive while $\mu^+ \to e^+\gamma$ has little sensitivity. The Mu2e experiment can probe an effective mass scale up to $\boldsymbol{O}(10^4\,\text{TeV})$. If there is null result from MEG-II, there is still an opportunity to observe $\mu^- N \to e^- N$ signal in Mu2e, because of the potential existence of non-photonic contributions.

2.2 The Mu2e Experiment

The Mu2e experiment at Fermilab is designed to search for coherent conversion of muons into electrons in the field of a nucleus ($\mu^- N \to e^- N$), as an example of Charged Lepton Flavor Violation (CLFV), which has never been observed before.

In the Mu2e experiment, the low momentum muons are stopped in a stopping target, and form muonic atoms. Then the muonic atoms cascade down to the 1s state rapidly. The muonic atoms decay after a certain lifetime through two major processes: muon decay-in-orbit (DIO) and muon captured by nucleus. Both the lifetime and ratio between two processes are dependent on the material of stopping target. The Mu2e experiment adopts

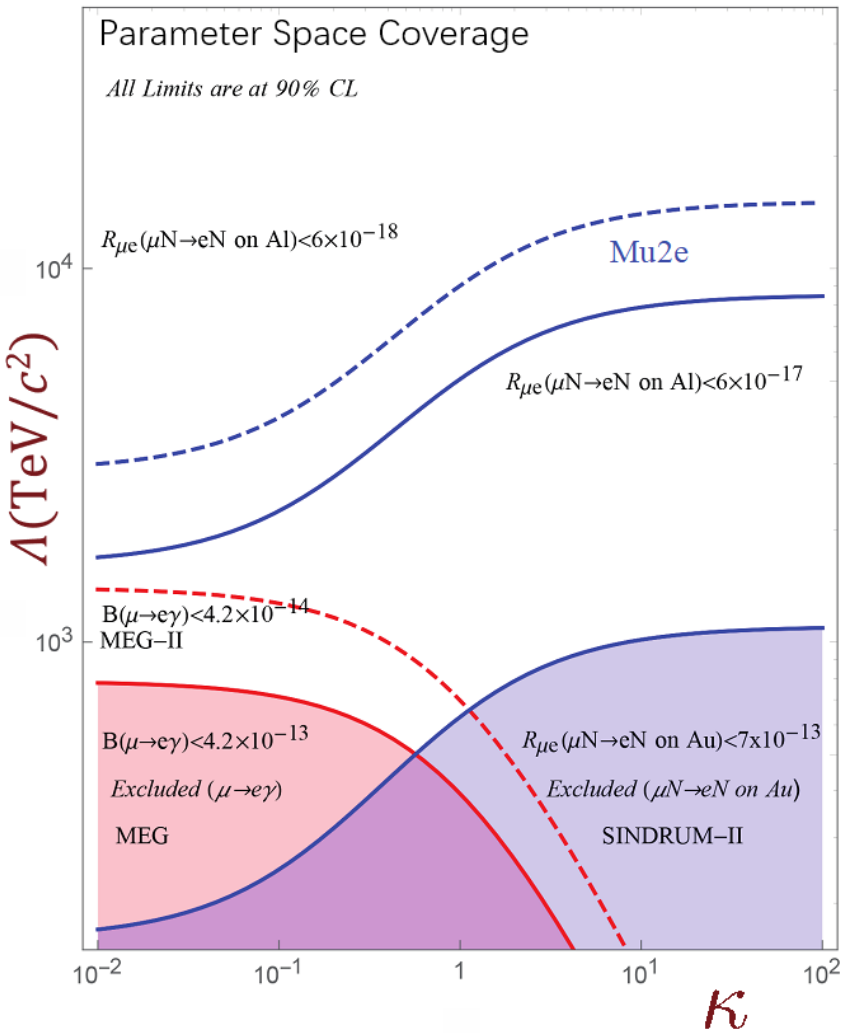

Figure 2.3. CLFV Lagrangian parameter space covered by past and upcoming muon rare decay experiments. The solid and dashed lines correspond to certain branching ratios in respective decay modes.

aluminum stopping target, and the lifetime of muonic atom is 864 ns. For aluminum, the branch ratio of the two processes are:

- The muon decays in orbit (DIO) ($\sim 40\%$): the muon decays to an electron, an electron antineutrino, and a muon neutrino. $\mu^- N \to \mathrm{e}^- N \nu_\mu \bar{\nu}_\mathrm{e}$
- The muon is captured by an Al nucleus($\sim 60\%$), which produces a magnesium nucleus and a muon neutrino. $\mu^- + A(Z,N) \to \nu_\mu + A(Z-1,N)$

The Mu2e experiment searches for a third decay mode, the neutrinoless muon-to-electron conversion ($\mu^- N \rightarrow e^- N$), which has the distinctive signature of a single monoenergetic electron with the energy evaluated as:

$$E_{\mu e} = m_\mu c^2 - (\text{B.E.})_{1s} - E_{\text{recoil}} = 104.97 \text{ MeV} \tag{2.3}$$

Here m_μ is the rest mass of muon, $(\text{B.E.})_{1s}$ is the binding energy of the muonic 1s state, and E_{recoil} is the energy of the nuclear recoil. Finally, the Mu2e experiment will measure or set stringent limits on the ratio of the rate of the neutrinoless, coherent conversion of muons into electrons in the field of a nucleus, relative to the rate of ordinary muon capture by the nucleus [1]:

$$R_{\mu e} = \frac{\mu^- + A(Z,N) \rightarrow e^- + A(Z,N)}{\mu^- + A(Z,N) \rightarrow \nu_\mu + A(Z-1,N)}$$

The current upper limit of the muon-to-electron conversion ratio, $R_{\mu e} < 7 \times 10^{-13}$ (90% CL), is given by the SINDRUM II experiment [18]. The Mu2e experiment aims to reach a single event sensitivity of 3×10^{-17}. If no signal is observed, the Mu2e experiment will set an upper limit on $R_{\mu e}(\mu^- \text{Al} \rightarrow e^- \text{Al}) < 8 \times 10^{-17}$ (90% CL), which improves the current limit by four orders of magnitude.

2.2.1 Mu2e Apparatus

A schematic overview of the Mu2e apparatus is shown in Figure 2.4. It consists of three parts: Production Solenoid, Transport Solenoid and Detector Solenoid.

- **Production Solenoid**: The production solenoid produces a graded magnetic field varying smoothly from 4.6 Tesla to 2.5 Tesla and surrounds the production target. The production target is made of tungsten. The 8 GeV pulsed proton beam from the Fermilab accelerator complex will strike the production target near the center of the Production Solenoid, producing mostly pions. The pions are short-lived and decay to muons in flight. Low momentum forward going pions will be reversed by the gradient magnetic field, and together with back-scattered pions travel to the transport solenoid.

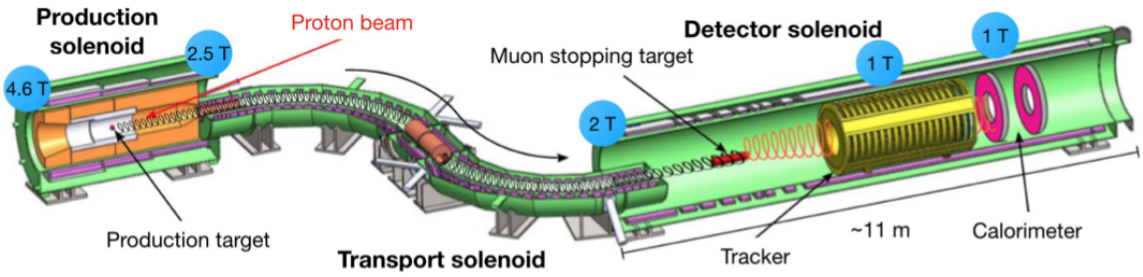

Figure 2.4. The schematic of the Mu2e apparatus. An 8 GeV proton beam strikes the production target, pions are produced and decay into muons. Low momentum μ^- are transferred to DS and stopped in the stopping target. The tracker and calorimeter, located in a uniform 1 T magnetic field, measure the conversion electrons momentum and energy, respectively.

- **Transport Solenoid**: The Transport Solenoid (Figure 2.5) is designed to maximize the stopped muon yield by efficiently focusing the charged particles created in the Production Solenoid towards the stopping target located in the Detector Solenoid. It is characterized by an S-shape, long enough to allow the decay of all hadrons while two 90° curved toroid sections (TS2 and TS4) eliminating the neutral particles. As the charged particles travel through the first curved toroid section (TS2), they will drift in opposite perpendicular directions as shown in Figure 2.6. A collimator with a vertically displaced aperture resides in the central straight section (TS3) and performs a sign and momentum selection, resulting in a low momentum, negatively charged beam. The second toroid section (TS4) returns the negatively charged beam close to the solenoid axis. TS1 and TS5 are also equipped with collimators for momentum selection.

- **Detector Solenoid**: The Detector Solenoid is a large, low field magnet that houses the muon stopping target and the detectors to identify and analyze conversion electrons from the stopping target. The stopping target, which consists of 37 thin aluminum foils, is located in a graded field that varies from 2 to 1 Tesla. The graded magnetic field can reverse the conversion electrons (CE) emitted upstream to the opposite direction

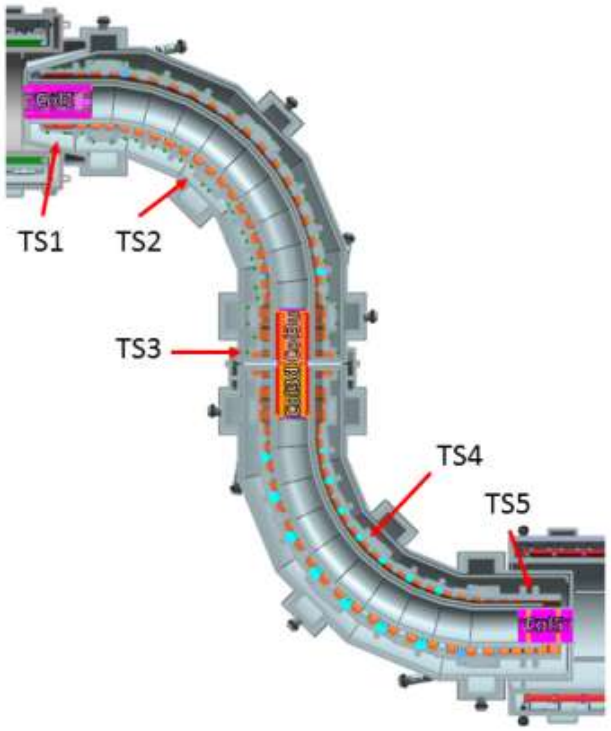

Figure 2.5. The Transport Solenoid consists of a set of superconducting solenoids and toroids that efficiently transmits low momentum negative muons.

towards the tracker. It can also focus the CE into a narrow range of pitch angle, which is extremely useful for the pattern recognition of reconstructed tracks. Momentum of the charged particles from decays of muons stopped in the stopping target are measured by the tracker, located in the uniform 1T magnetic field. The tracker consists of 21600 mylar low-mass straw-tubes aligned transverse to the DS axis and arranged into 36 panels (Figure 2.7). The active area of the tracker covers about $40 < r < 70$ cm, where the radius r is measured from the DS axis. This design is optimized to maximize the acceptance to conversion electrons while minimizing the number of low momentum electrons intercepted by the tracker (Figure 2.7). The tracker is expected to provide a momentum resolution of ~ 100 keV/c at the CE momentum of 105 MeV/c.

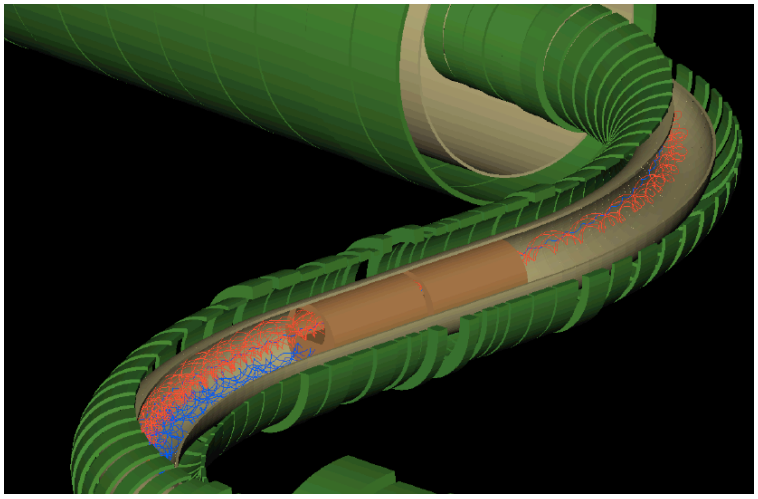

Figure 2.6. As the charged particles traverse the first curved toroid section of the Transport Solenoid, they will disperse in opposite vertical directions by charge. The central collimator absorbs the positive particles (blue) while allowing the negative particles (red) within a particular momentum window to pass through.

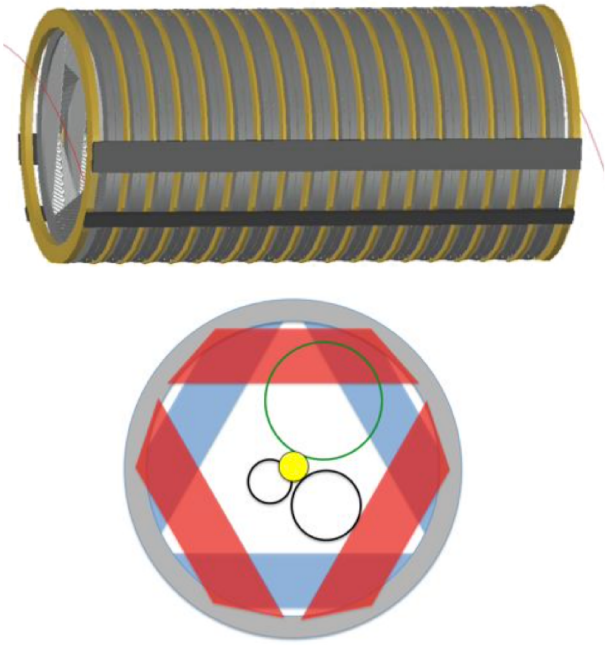

Figure 2.7. (top) The Mu2e straw tube tracker and (bottom) the acceptance of the annular design to the radii of 105 MeV/c conversion electrons (green) and lower momentum backgrounds (black) emitted from the stopping target.

2.3 Mu2e Background and Momentum Scale

There are a number of background processes that can generate 105 MeV electrons:

- Decays in orbit (DIO) of muons in muonic atoms produce electrons with a momentum spectrum extending up to E_{CE} and rapidly falling towards the spectrum endpoint. This is demonstrated graphically in Figure 2.8.

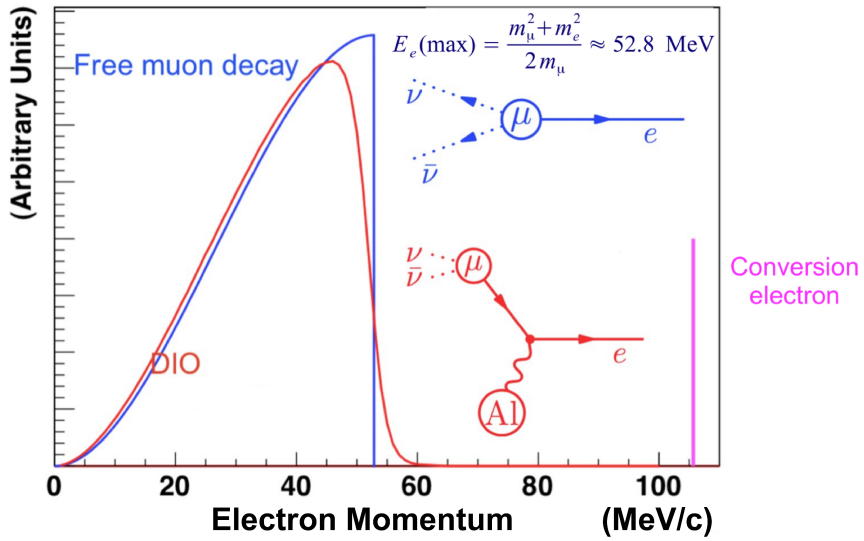

Figure 2.8. Qualitative representation of electron momentum spectrum due to free muon decay (blue), muon decay-in-orbit (red), and conversion electrons (magenta).

- Antiprotons produced by the proton beam and annihilating in the stopping target generate $\sim$ 100 MeV/c electrons. The antiproton background is suppressed by several absorption elements in the TS.

- Radiative capture of pions (RPC) background: Radiative processes where the stopped pion is captured by the Al nucleus and radiates a photon, which then undergoes electron-positron pair production. This process falls rapidly in time. Suppressing the RPC background requires the signal window to be delayed with respect to the proton arrival at the production target by several hundred nanoseconds, as shown in Figure 2.9.

- Cosmic particles interacting and decaying in the detector volume are a source of electrons with momentum spectrum covers the region $\sim$ 100 MeV/c. Most cosmic particles entering the detector volume are muons. Suppressing the cosmic background requires the Cosmic Ray Veto system (CRV) to identify muons and veto them.

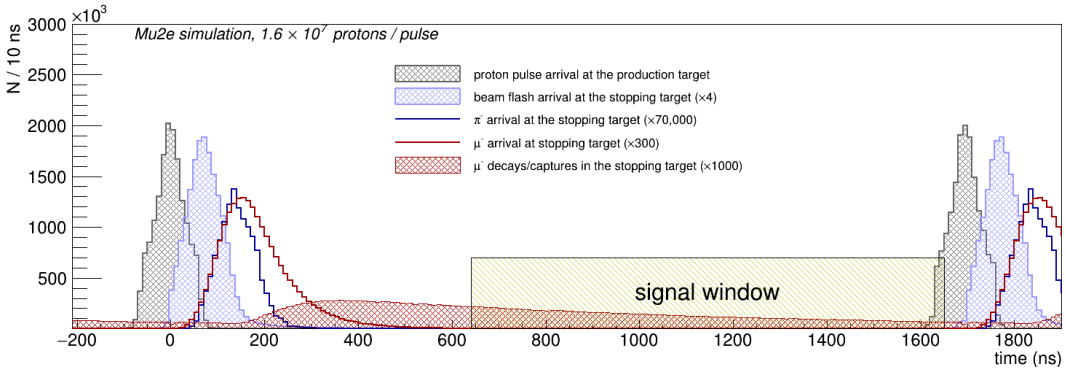

Figure 2.9. Timing distributions for the CE signal and various backgrounds, with the signal window delayed after the reduction of prompt backgrounds.

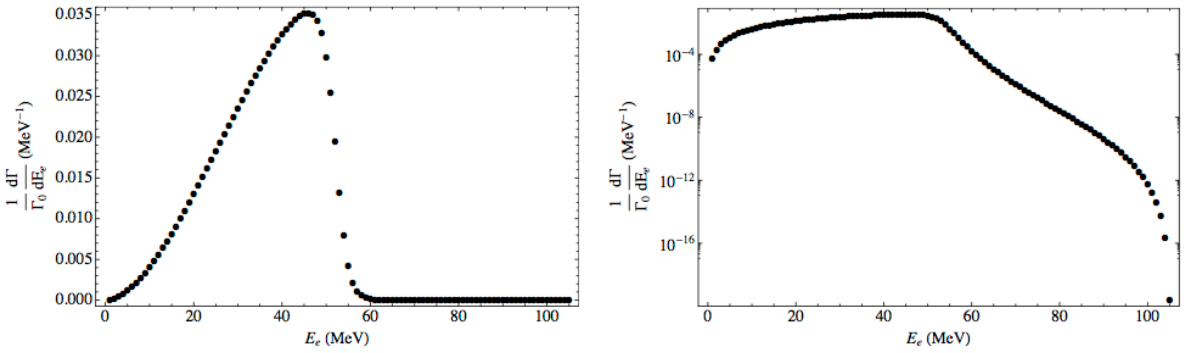

Figure 2.10. Theoretical energy spectrum for electrons from muon DIO on aluminum on a linear (left) and log (right) scale.

The primary background of concern comes from DIO events, since the time distribution of DIO events is identical to that of a potential conversion electron (CE), which makes it an irreducible physics background for Mu2e. To accurately estimate the DIO background, we must have a good understanding of the energy spectrum of the DIO. The theoretical calculation of the DIO electron energy spectrum [30] is shown in Figure 2.10. The spectrum

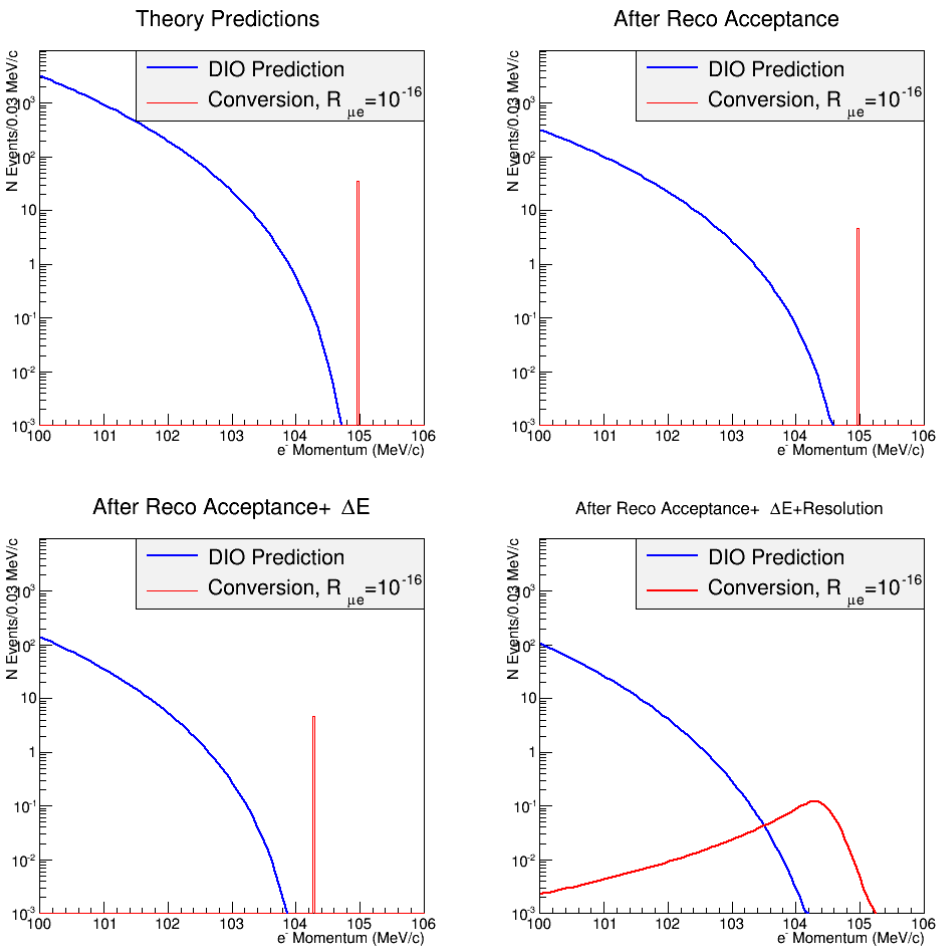

Figure 2.11. Upper left are theoretical predictions. Upper right are after applying realistic detector acceptances. Lower left is after acceptance and average energy loss effects. Lower right is after all reconstruction effects.

in Figure 2.10 will be reshaped by experimental effects such as energy loss, tracker acceptance and reconstruction effects. Figure 2.11 shows how various experimental effects reshape the momentum spectrum of DIO background and signal CE. Electrons produced in the stopping target will interact with materials upstream of the tracker such as stopping target, inner proton absorber and outer proton absorber. Figure 2.12 shows the momentum spectrum of conversion electrons originated in the stopping target (green), at a point just upstream of the tracker (blue), reconstructed in the tracker (red). The long negative tail comes from radiative energy loss (Bremsstrahlung), while the core width comes mostly from straggling in the

ionization energy loss. The largest material interaction energy loss comes from the stopping target. The design of the stopping target has been optimized to balance the effects of stopping efficiency for muons and energy degradation for conversion electrons. Another material upstream of the tracker is the inner proton absorber, which slows or stops the protons produced in nuclear decay following muon capture, thereby protecting the tracker from high hit rates and large charge deposition. The energy loss in the tracker further broadens the spectrum and the high-side tail above 105 MeV/c is caused by misreconstruction.

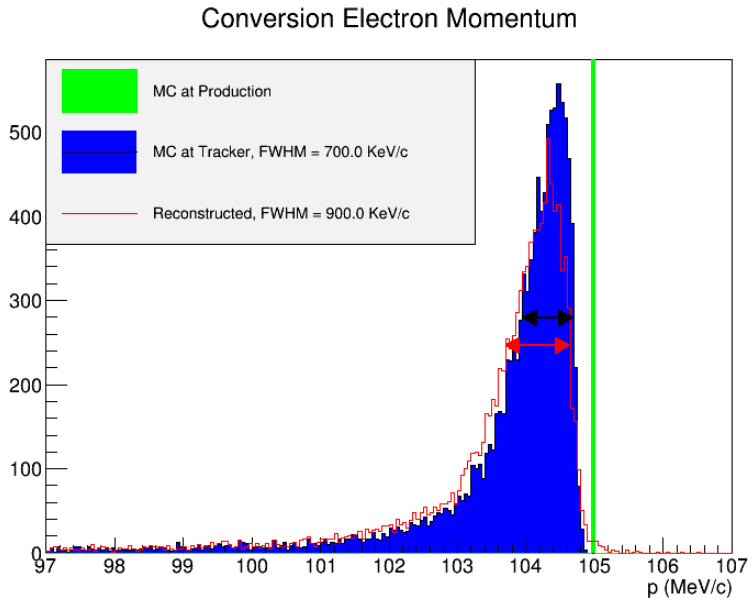

Figure 2.12. The momentum spectrum of conversion electrons estimated by a detailed GEANT4 simulation of the Mu2e apparatus. The spectra at production (green), after interaction in upstream material (blue), and after reconstruction (red).

An overlay of reconstructed DIO and potential CE momenta by simulation is shown in Figure 2.13, assuming $R_{\mu e} = 1 \times 10^{-16}$. Both distributions are normalized to 6.7×10^{17} muon stops expected for the full nominal Mu2e run. To reduce the impact of DIO background on the single event sensitivity of the experiment, Mu2e requires less than 0.2 DIO events for the full nominal Mu2e run, within an error of 0.05 events. Therefore, we select the tracks with momentum between 103.75 and 105.00 MeV/c. The integral of DIO background is 0.22 ± 0.03 events, and the integral of CE signal is 3.8 ± 0.03 events. There are also several

effects that contribute to the systematic uncertainty of DIO background yield. The major effects come from the theoretical calculation of the DIO spectrum, and the range of the absolute momentum scale of reconstructed tracks.

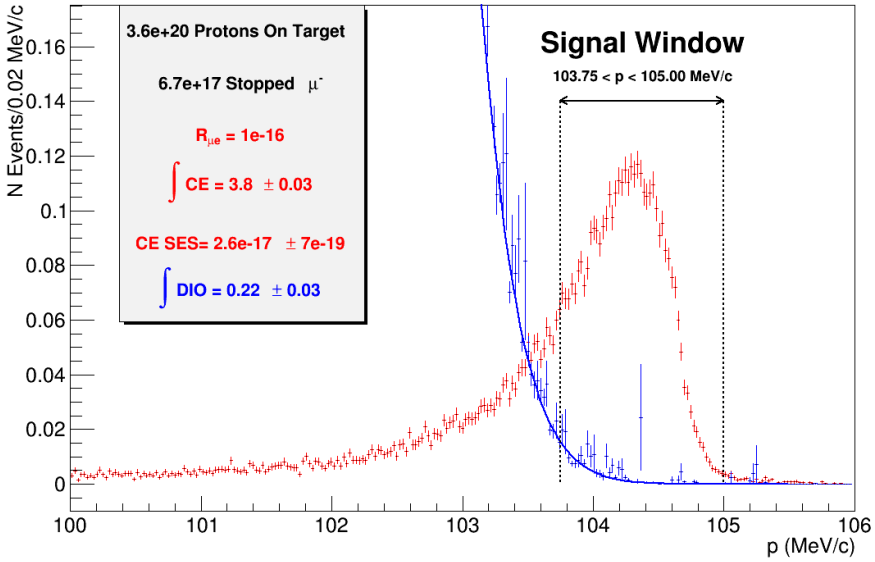

Figure 2.13. The reconstructed momenta spectrum for DIO background (Blue) and conversion electron (CE) signal (Red) surviving the track selection criteria, assuming $R_{\mu e} = 1 \times 10^{-16}$. The two vertical dashed lines indicate the momentum search window, 103.75 < P < 105.00 MeV/c.

Figure 2.14a shows the changes in the DIO and CE rates for the nominal momentum signal window, as a function of a putative shift in the momentum. To satisfy the DIO rate uncertainty be < 0.05 events, the required accuracy on the absolute momentum scale will be about ±60 keV/c, which would be very difficult to achieve. If we shift up the momentum signal window by 100 keV/c, the momentum scale accuracy required to achieve < 0.05 events DIO rate uncertainty will be ±100 keV/c. Therefore, we adopt a 100 keV/c accuracy requirement on the absolute momentum scale.

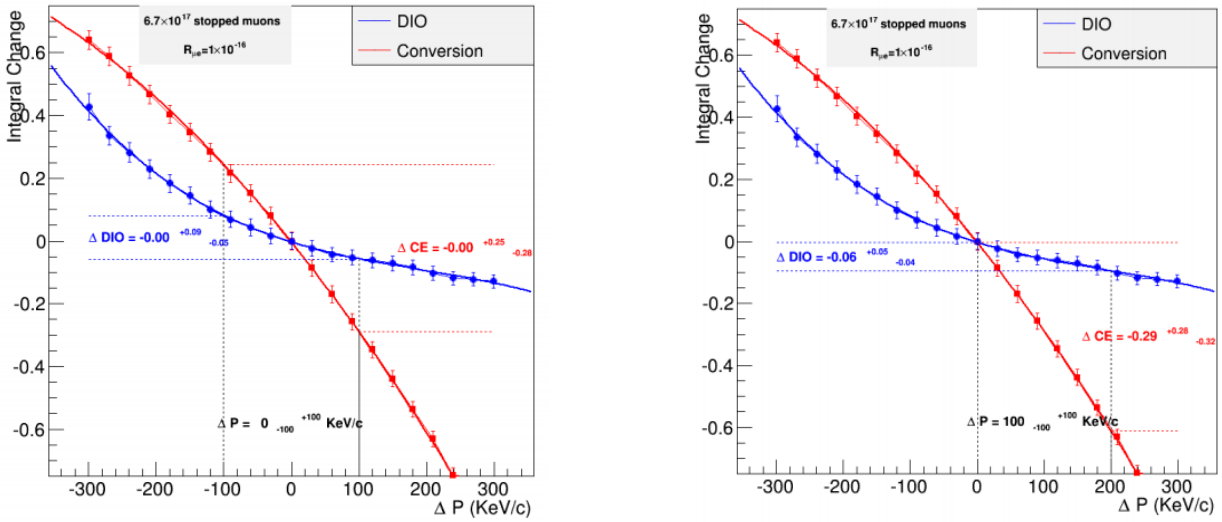

(a) (b)

Figure 2.14. Integral changes in the DIO and CE yields for the (a) nominal momentum signal window and (b) momentum signal window that has been shifted up by 100 keV/c, as a function of a putative shift in the momentum. The changes corresponding to an uncertainty of 100 keV/c on the momentum scale are illustrated.

3. CALIBRATION

As we discussed in the last chapter, the accuracy of the momentum scale makes the dominant systematic uncertainty on the DIO background. We expect the momentum scale of the Mu2e tracker to be calibrated to an accuracy of better than 100 keV/c at p = 100 MeV/c. However, the DIO background doesn't have a spectrum feature that can be used for calibration. Therefore, the Mu2e detector's response needs independent calibration to verify the scale and accuracy of the reconstructed momentum spectrum. The particle source for the calibration should satisfy the following criteria:(a) the particle source can be easily achieved in a high rate by some configuration changes to the nominal Mu2e experiment setup. (b) the particle source generates the signal (electron or positron) with a narrow peak or sharp edge in the momentum spectrum after interacting with the stopping target. (c) the backgrounds should be low or can be excluded by the track selection.

There are a number of potential techniques for calibration:

- Measurement of the mono-energetic positrons at $\sim$ 70 MeV/c from $\pi^+ \to e^+\nu_e$ decays of stopped pions in the stopping target. The tracker acceptance for this physics process is optimized at the tracker field of 0.7 T. Moreover, a dedicated run with a reversed charge selection through the collimator rotation in the TS, and a time window change is needed.

- Reconstruction of the DIO electrons spectrum edge at $\sim$ 50 MeV/c from $\mu^- \to e^-\bar{\nu}_e\nu_\mu$. The tracker acceptance for this physics process is optimized at the tracker field of 0.5 T. Moreover, a reduced proton beam intensity is needed.

- Reconstruction of the Michel positrons spectrum edge at $\sim$ 52.8 MeV/c from stopped $\mu^+ \to e^+\nu_e\bar{\nu}_\mu$. The Michel positrons spectrum edge is much sharper than that of the DIO electrons. The tracker acceptance for this physics process is optimized at the tracker field of 0.5 T. Moreover, a reduced proton beam intensity, and a reversed charge selection through the collimator rotation in the TS are needed [31].

- Electrons produced by the cosmic rays in the calorimeter which are reconstructed in the tracker both upstream and downstream. Reflecting particles are reconstructed as two separate tracks, once on the upstream path and again on the downstream path. The difference in the reconstructed momentum values of these tracks can be fitted to extract the momentum resolution and shift, over a broad range of momentum, angle, and position in the tracker.

The mono-energetic 69.8 MeV/c positrons e^+ from the decays of positively-charged pions ($\pi^+ \rightarrow e^+\nu_e$) that have stopped in the aluminum stopping target are investigated as a calibration source to measure the absolute momentum scale and momentum resolution. The small momentum smearing caused by radiative corrections ($\pi^+ \rightarrow e^+\nu_e\gamma$) is well studied theoretically in [32] and measured experimentally in [33]. The BR($\pi^+ \rightarrow e^+\nu_e$) $\approx 1.23 \times 10^{-4}$ and BR($\pi^+ \rightarrow e^+\nu_e\gamma$) $\approx 7.39 \times 10^{-7}$, thus the correction is at the level of 10^{-2}.

3.1 Configuration

In the nominal Mu2e experiment, negative particles are selected by the TS and negative muons are stopped at the aluminum stopping target. The Mu2e signal is mono-energetic $\sim$ 105 MeV/c electrons, which are measured by the straw tracker and the calorimeter in the downstream of the DS. Both detectors have acceptance only for particles with momentum P $>$ 70 MeV/c to avoid overwhelming both the straw tube total charge load and the reconstruction capability of the tracker.

The momentum calibration using stopped $\pi^+ \rightarrow e^+\nu_e$ decay requires some configuration changes to the nominal Mu2e setup:

- The transport solenoid needs to be configured to allow π^+ beam transport to the stopping target, and reject negatively charged particles.

- The start time of signal window needs to be moved to a earlier time since the lifetime of pion is much shorter than that of the muonic atom.

- The magnetic field of the detector solenoid needs to be reduced to allow 70 MeV/c positrons to enter the tracker with a high acceptance.

3.1.1 Selecting π^+ in TS

The Transport Solenoid is designed to allow the selected charge sign particles to pass through. As the charged particles traverse the first curved toroid section of the Transport Solenoid, they will disperse in opposite vertical directions by charge (as shown in Figure 2.6). There is a rotatable charge-selecting collimator inserted at the center of the Transport Solenoid to allow only negatively charged particles to pass through in the nominal Mu2e experiment [1]. The position of charge-selecting collimator in TS and its dimensions are shown in Figure 3.1. In the calibration run, the charge-selecting collimator will be rotated 180 degrees to allow positive particles travel through.

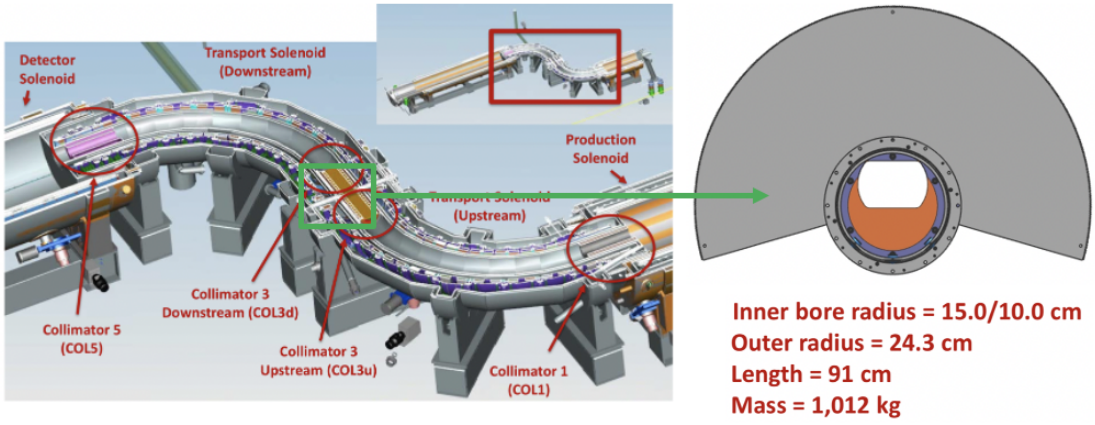

Figure 3.1. (Left) The position of the charge-selecting collimator within the Transport Solenoid (Right) The design of collimator in cross section and its dimensions.

3.1.2 Lowering Signal Window to 200 ns

In the nominal Mu2e experiment, negative muons and aluminum nuclei form muonic atoms with a mean lifetime of $\sim$ 864 ns. A delayed signal window, starting from 650 ns, suppresses the beam-related background (as shown in Figure 2.9). In the calibration run using $\pi^+ \rightarrow e^+\nu_e$, pions arrive at the stopping target at $\sim$ 150 ns in average after proton hit on the Production Target (as shown in Figure 3.2), and the stopped pions are short-lived with a mean lifetime of 26 ns, which is much shorter than the lifetime of muonic atoms.

Therefore, we need to lower the start time of the signal window to the arrival time of pions at the stopping target. We set the signal window start from 200 ns to suppress background related to beam flash (blue shaded in Figure 3.2). The beam flash contains the secondary particles other than π and μ, arriving at the stopping target. Another key observation from Figure 3.2 is that the muon arrival time at the stopping target (red solid) overlaps with that of pions (blue solid), and the rate of muons is much larger than that of pions. Thus, the muon decay-in-flight (DIF) process is one of the backgrounds in concern.

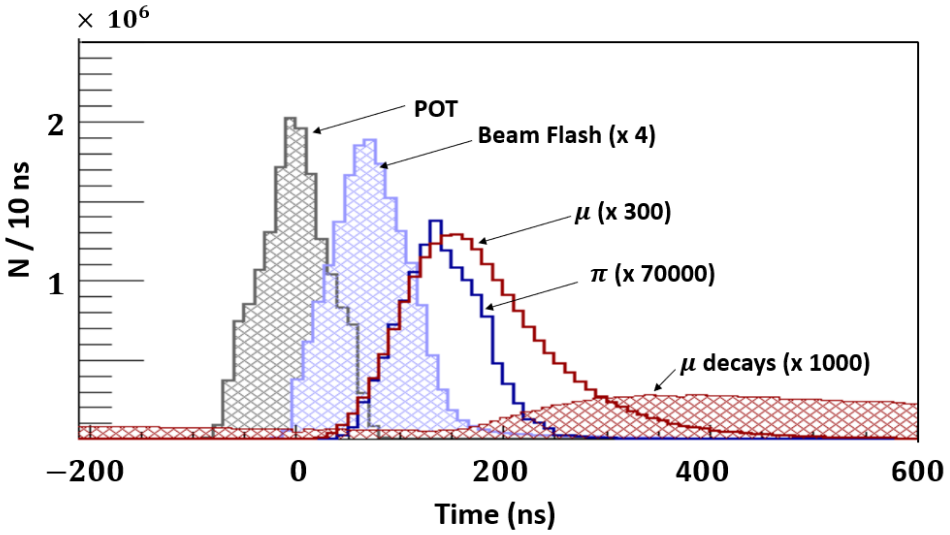

Figure 3.2. Number of particles arriving at the production target/ stopping target as a function of time for one beam pulse of 1.6×10^7 protons on target (POT). The grey shaded shows one proton beam pulse on the production target. The beam flash (blue shaded) contains the secondary particles other than π and μ, arriving at the stopping target. The pions (blue solid) and muons (red solid) arrive at the stopping target with a time delay. The red shaded shows the the number of stopped muons that decay-at-rest in the stopping target. Adapted from Figure 2 in Ref. [2].

3.1.3 70% Reduced Magnetic Field in DS

The magnetic field of upstream detector solenoid varies from 2 Tesla to 1 Tesla and surrounds the stopping target. The tracker and calorimeter locate in a uniform 1 T magnetic field downstream [34]. The magnetic field of the detector solenoid points toward the z-axis,

parallel to the axis of the stopping target, tracker and calorimeter, as shown in Figure 3.3. The calibration run requires reduced B-field of the detector solenoid to allow signal positrons to enter the tracker with a high acceptance fraction. The helical radius of the particle trajectory in the magnetic field R $\propto$ P/B, where P is the momentum of track. To keep the radius of signal positrons ($\sim$ 70 MeV/c) same as that of the Mu2e conversion electrons (CE) signal ($\sim$ 105 MeV/c), we need to reduce the magnetic field of the detector solenoid to 70% of nominal, while keeping the magnetic field of the upstream production and transport solenoid at the nominal strength. The strength of the magnetic field is controlled by the current flow in the surrounding superconducting coils. The 70% reduced field can be achieved by reducing the current flow to 70% of nominal in the DS.

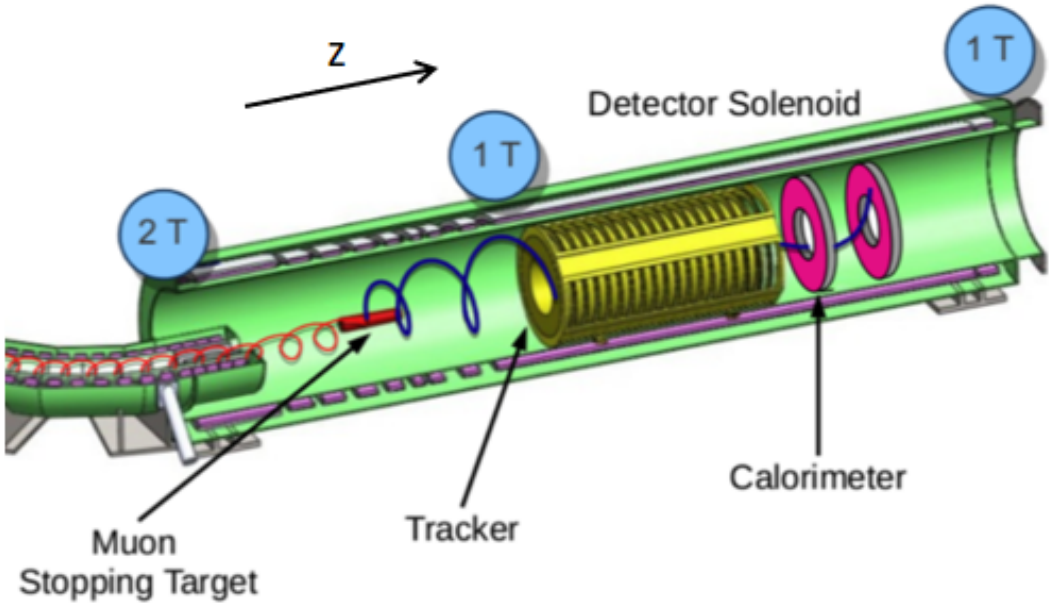

Figure 3.3. The magnetic field of the detector solenoid points toward the z-axis, parallel to the axis of the stopping target, tracker and calorimeter.

3.2 Degrader

In the nominal Mu2e experiment, the mass of the stopping target is optimized for stopping μ, however, the π momentum spectrum is much higher than μ, resulting in most of the π-beam

passing straight through the target if their momenta is not reduced beforehand. Therefore, it's necessary to place a degrader material upstream of the stopping target to increase the number of stopped π in the stopping target. Figure 3.4 shows the position of the degrader in the DS. The material of the degrader is chosen to be titanium (Ti) based on the following reasons: (a) it cannot be aluminum material, since extra aluminum will contribute to the DIO background in the nominal Mu2e experiment. (b) The Ti is a low-Z material, so any small difference in material thickness between the simulation and the constructed degrader would very minimally affect the π stops distribution. (c) The Ti material is easy to machined into the degrader.

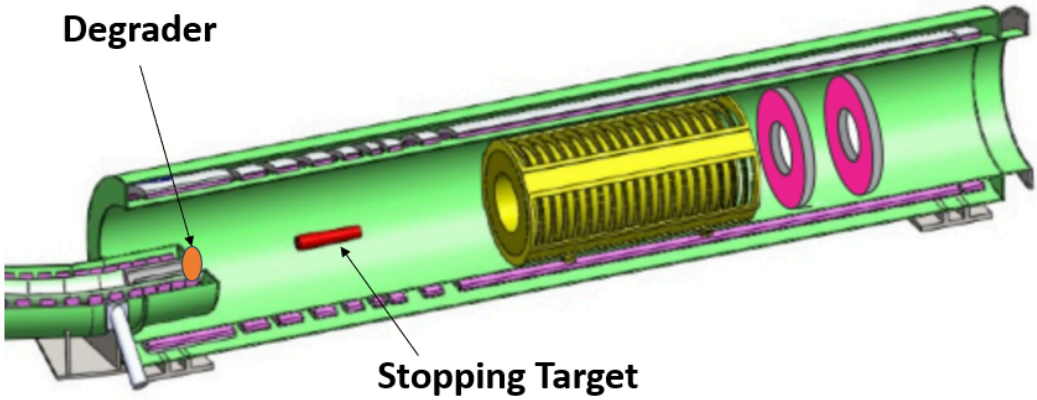

Figure 3.4. The position of degrader relative to the stopping target in the DS.

3.2.1 Optimization on Pion Stops

We simulate the π stops in the stopping target using a new and validated version of the Mu2e Offline software framework, and calculate the pion stops in the stopping target as a function of degrader thickness. Figure 3.5 shows the pion stops efficiency as a function of degrader thickness, where the pion stops efficiency is defined as the number of pion stops in the stopping target per proton-on-target normalized to 2mm Ti case. The number of pion stops in the stopping target is maximized with the 2mm Ti degrader.

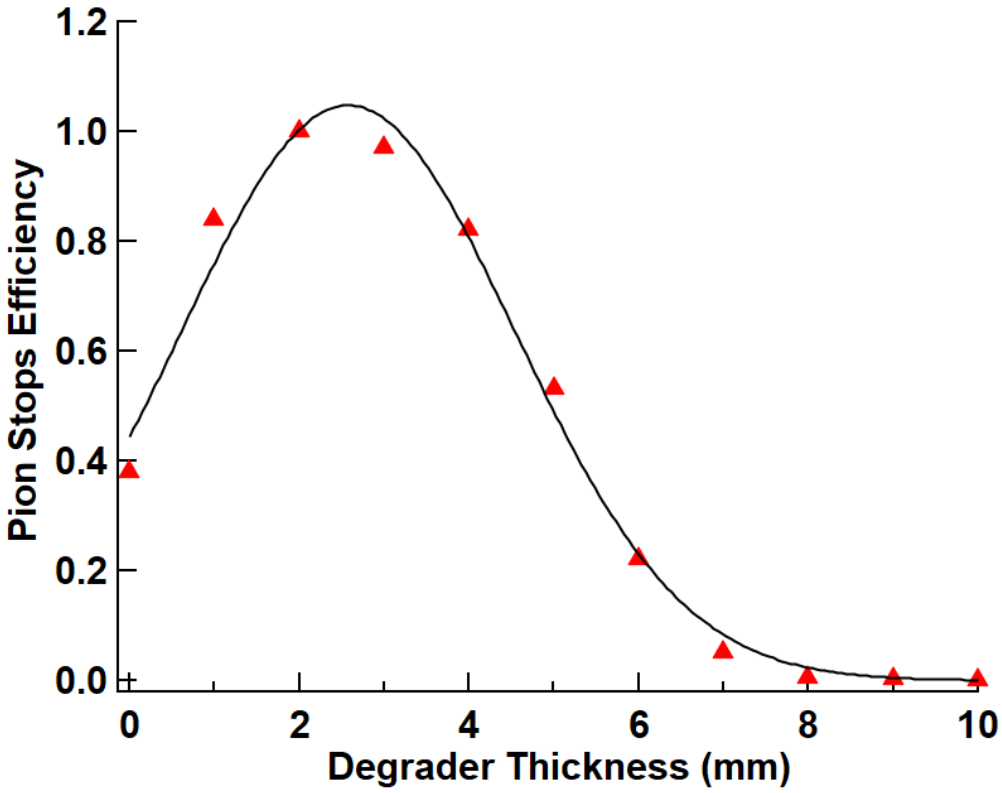

Figure 3.5. The pion stops efficiency as a function of degrader thickness. The black curve is given by Gaussian fitting.

3.2.2 Calibration Backgrounds

In this section, the backgrounds in the calibration run are discussed qualitatively. The backgrounds for the calibration arise from beam-backgrounds and other stopped π^+ decays that produce reconstructed e^+ tracks mimicking a signal trajectory originating from the stopping target:

- The beam-backgrounds originate from beam particles such as μ^+ as well as π^+ that enter the DS and produce decay particles in flight that are then reconstructed.
- Stopped $\pi^+ \to e^+$ in degrader
- Stopped $\pi^+ \to \mu^+$ in stopping target and degrader

For the beam-backgrounds, the dominant case is a pion produced in the production solenoid and decays to a muon shortly, the the muon passes through the degrader into the DS and decays in flight to a positron with a momentum at or near the expected 70 MeV/c calibration signal that are then reconstructed. Therefore, we also call the beam-backgrounds as the μ decay-in-flight (DIF) background in the later chapters. For the stopped $\pi^+ \to e^+$ in degrader background, it generates mono-energetic 69.8 MeV/c positrons starting from the degrader. The graded field in the upstream of the DS will reduce the polar angle θ as the particle travels downstream, where θ is the angle between momentum vector and the DS axis. Since the background positrons start more upstream than the signal positrons, the polar angle θ of the background tracks entering the tracker will be smaller than that of the signal tracks. Therefore, we can suppress the stopped $\pi^+ \to e^+$ in degrader background by applying appropriate selection cut on the θ of the reconstructed tracks. For the stopped $\pi^+ \to \mu^+$ in stopping target and degrader background, the decay of stopped pions generate mono-energetic $\sim$ 30 MeV/c muons. Note that 30 MeV/c is the minimum momentum of the muon that can decay to a positron with momentum at $\sim$ 70 MeV/c, when in the $\mu^+ \to e^+\nu\nu$ process, two neutrinos are ejected in the same direction opposite to the positron. Therefore, the e^+ momentum spectrum from stopped $\pi^+ \to \mu^+$ background ends at 70 MeV/c. The contribution of the stopped $\pi^+ \to \mu^+$ background must be smaller than that of the μ-DIF background.

The most significant background is the aforementioned $\mu^+ \to e^+\nu\nu$ decay-in-flight where the e^+ track is reconstructed in the Mu2e detectors with a momentum at or near the expected 70 MeV/c calibration signal. The degrader can significantly reduce the incoming μ^+ momentum spectrum, consequently reducing the impact of μ decay-in-flight background. The momentum spectrum of the muons entering the DS are simulated with different degrader thickness. Figure 3.6 shows the muon flux efficiency as a function of degrader thickness, where the muon flux efficiency is defined as the number of muons with momentum larger than 30 MeV/c entering the DS per proton-on-target normalized to 2mm Ti case.

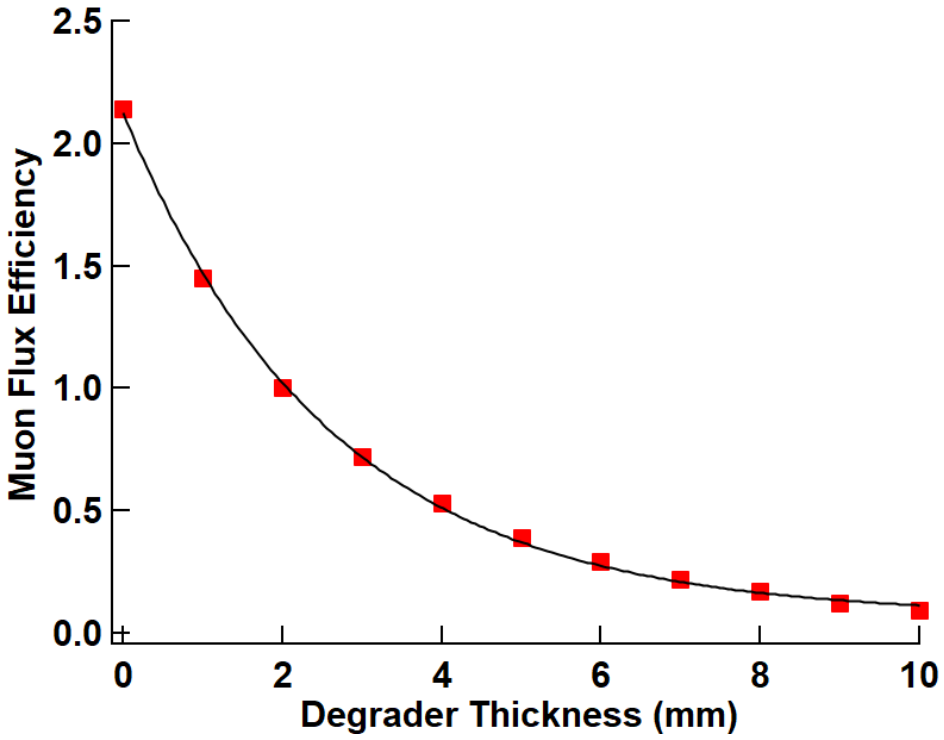

Figure 3.6. The muon flux efficiency as a function of degrader thickness. The black curve is given by exponential fitting.

3.2.3 Optimized Degrader Thickness

The ratio of S/B is used as a figure of merit. Thus, the Ti degrader thickness is optimized by the pion stops efficiency to muon flux efficiency ratio. Figure 3.7 shows the ratio as a function of degrader thickness. The ratio peaks at 4mm, so we conclude that the 4mm Ti degrader can make the largest signal-to-background ratio for this calibration mode. The 4 mm Ti degrader can further reduce the μ-DIF background by a factor of ~ 2 at the cost of 18% pion stops loss in the stopping target compared to the 2mm Ti degrader.

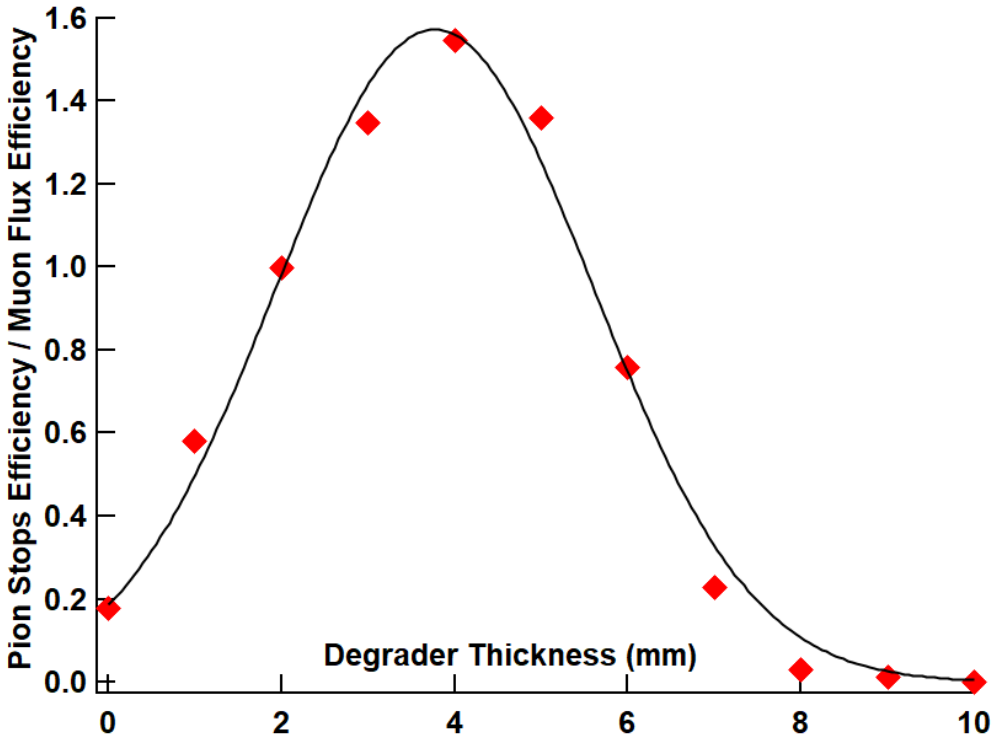

Figure 3.7. The pion stops efficiency to muon flux efficiency ratio as a function of degrader thickness.The black curve is given by Gaussian fitting.

4. SIMULATION METHODS

Mu2e Offline is a collection of code and scripts used for simulation, reconstruction and analysis of Mu2e data. The Mu2e Offline simulation framework is based on Geant4[3]–[5], which takes into consideration cross sections and time dependencies of the physics processes, response of the detectors, and effects of hit digitization and readout. Geant4 with the "QGSP_BERT" physics list is used as an underlying simulation engine for all simulations. The Mu2e apparatus are assumed perfectly aligned and calibrated for all simulations.

4.1 Staged Simulation and Resampling

The simulations run directly can be computationally expensive. Several techniques have been developed to make simulations efficiently, especially in minimizing CPU hours, disk space, and risk.

- Staging: Simulation can be interrupted at a certain point, output saved, and started again with resampling. The simulations are usually divided into three stages, in Production Solenoid, Transport Solenoid and Detector Solenoid. The staged simulation reduces the time loss risk due job crash by amount an order of magnitude and saves disk space by dropping unnecessary data products.

- Resampling: In staged simulation, we can save the output of a stage and simulate with resampling in the next stage. It works as long as there are significant variations in the simulation. For example, for the stopped $\pi^+ \to e^+\nu_e$ in the stopping target, a fairly small set of stopped pions can be used over and over again, since each event generates a positron that is launched into a different direction and makes very different hits in the tracker.

- For the simulation of stopped pion, the decay of pion is turned off. For the muon DIF simulation, the muons are forced to decay with shorter lifetime.

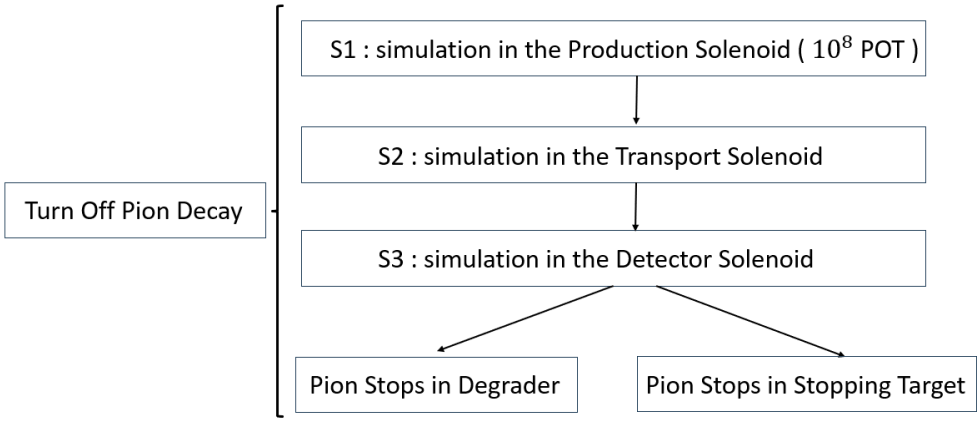

Figure 4.1. The diagram for the simulation of stopped pions in the stopping target and degrader.

4.1.1 Pion Stops

For the simulations of stopped $\pi^+ \to e^+$ or $\pi^+ \to \mu^+$ in stopping target and degrader, we first run the staged simulation displayed in Figure 4.1. The stopped pions are saved in the degrader and stopping target, which are then used as input for different case studies. In this study to make the simulation efficient, we turn off the pion decay and record the proper time of each stopped pion. We do this because the pion lifetime ($\sim$ 26 ns) is so short, most of pions decay into muons in S1 and S2. By weighing the pion stops with survival probability (calculated from the proper time), we can get the correct stopped pion position distributions in the stopping target and degrader. We only need to rerun S3 for different degrader thickness.

4.1.2 Stopped $\pi^+ \to e^+$ in Stopping Target and Degrader

We use the pion stops in the degrader and stopping target as input for the simulations, as shown in Figure 4.2. The pions are forced to decay into positrons. The branching fraction of $\pi^+ \to e^+$ decay mode is 1.23×10^{-4}. The reconstructed tracks are weighed by the survival probability of the corresponding stopped pion, its branching fraction and the resampling

factor. The stopped $\pi^+ \to e^+$ in the stopping target and degrader are simulated at the level of $O(10^{13})$ POT.

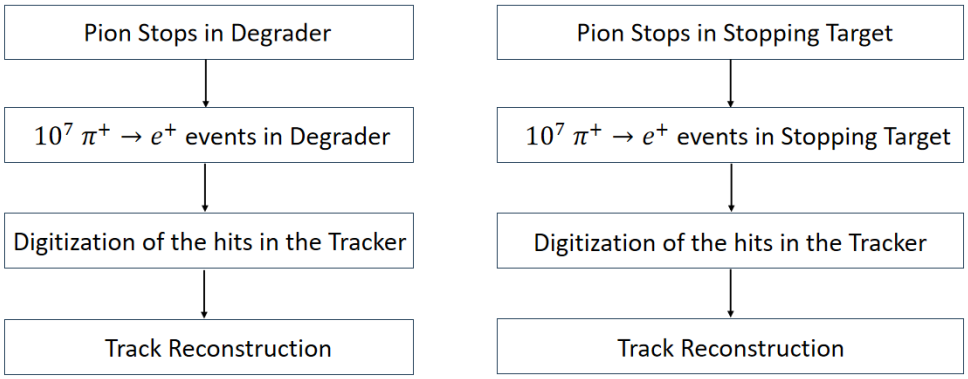

Figure 4.2. The diagram for the simulation of stopped $\pi^+ \to e^+$ in the stopping target and degrader.

4.1.3 Stopped $\pi^+ \to \mu^+$ in Stopping Target and Degrader

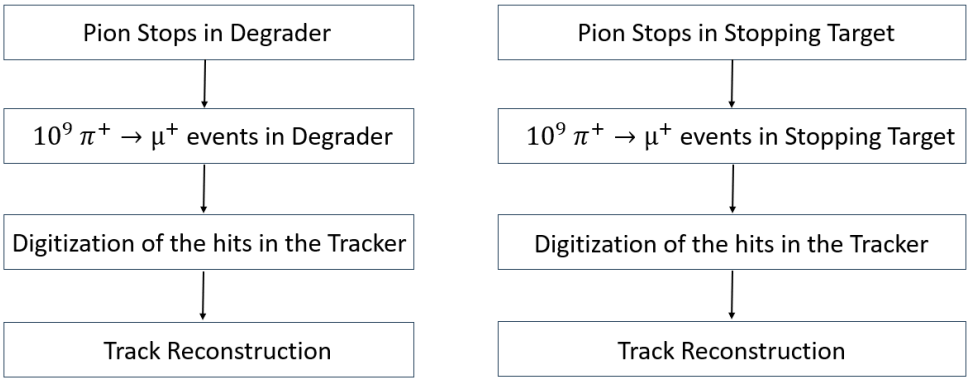

Figure 4.3. The diagram for the simulation of stopped $\pi^+ \to \mu^+$ in the stopping target and degrader.

For the backgrounds of the stopped $\pi^+ \to \mu^+$ in the stopping target and degrader, we use the pion stops in the degrader and stopping target as input for the simulation, as shown in Figure 4.3. As we discussed in Section 3.2.2, the momentum distributions of reconstructed tracks from these two backgrounds end at $\sim$ 70 MeV/c, we increase the number of events

to 10^9 to make continuous momentum distribution near $\sim$ 70 MeV/c. The pions are forced to decay into muons. The branching fraction of $\pi^+ \to \mu^+$ decay mode is 0.999877. The reconstructed tracks are weighed by the survival probability of the corresponding stopped pion, its branching fraction and the resampling factor. The stopped $\pi^+ \to \mu^+$ in the stopping target and degrader are simulated at the level of $O(10^{15})$ POT.

4.1.4 Muon Decay-in-Flight Background

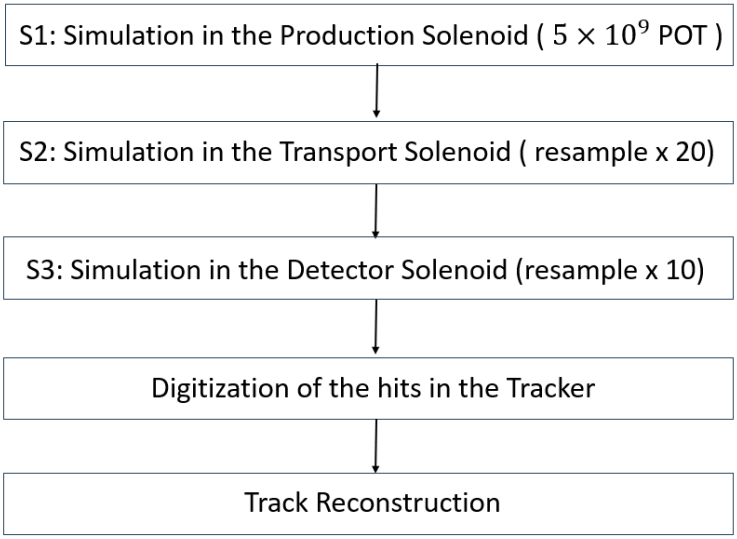

Figure 4.4. The diagram for the simulation of muon DIF background by the brute force method.

Figure 4.4 shows the staged simulation of muon decay-in-flight background by the brute force method, using a total number of 1×10^{12} events. The resampling factors are constrained by the available number of CPU hours. It takes about one week for a simulation with 10^{12} events. Even so we cannot get enough statistics near $\sim$ 70 MeV/c in order to understand the muon DIF background. Because the CPU time of the simulation increases linearly with the number of events, it is not efficient to get higher statistics using the brute force method.

4.2 Change the Proper Time of Muon

Due to the long lifetime of muon ($\sim$ 2197 ns), most of the muons just travel through the Detector Solenoid before decay. To further improve the efficiency of the muon DIF background simulation, we can shorten the lifetime of muon starting in the Detector Solenoid (S3), then get higher statistics using the reconstructed tracks caused by this shorter lifetime.

A new feature to set specific muon proper time was added in the Mu2e Offline. It can specify either a fixed muon proper time or min and max values of muon proper time. Figure 4.5 shows the restricted muon proper time distribution between 0-500 ns (Blue Area), on top of the standard muon proper time (Red Curve).

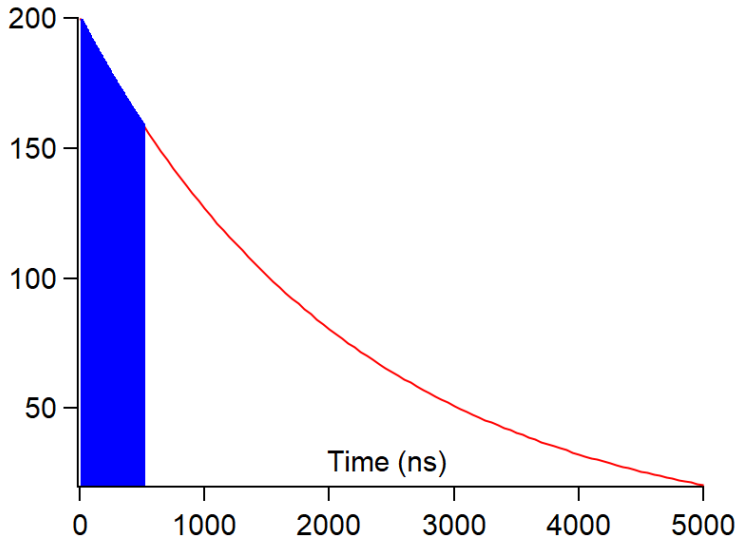

Figure 4.5. The distribution of standard proper time (at the decay time) of muon decaying at rest (Red Curve), with an overlayed distribution when the muon proper time is restricted to the range between 0 and 500 ns (Blue Area)

In the simulation of muon DIF background, we need to set max value of muon proper time that can cover all decay events in the Detector Solenoid (with normal muon lifetime). Figure 4.6 shows the muon decay position in the DS versus the proper time difference in DS with normal muon lifetime. We found that most muon decay events with reconstructed tracks happen between 0-150 ns and located in the region 4000-11000 mm (before or inside the Tracker). Figure 4.7 shows the Z position of the objects in Detector Solenoid using Mu2e

coordinates. Therefore, we can simulate the muon DIF background efficiently with restricted proper time between 0-150 ns, as shown in Figure 4.8. We also simulate the background with 150-300 ns proper time for completeness.

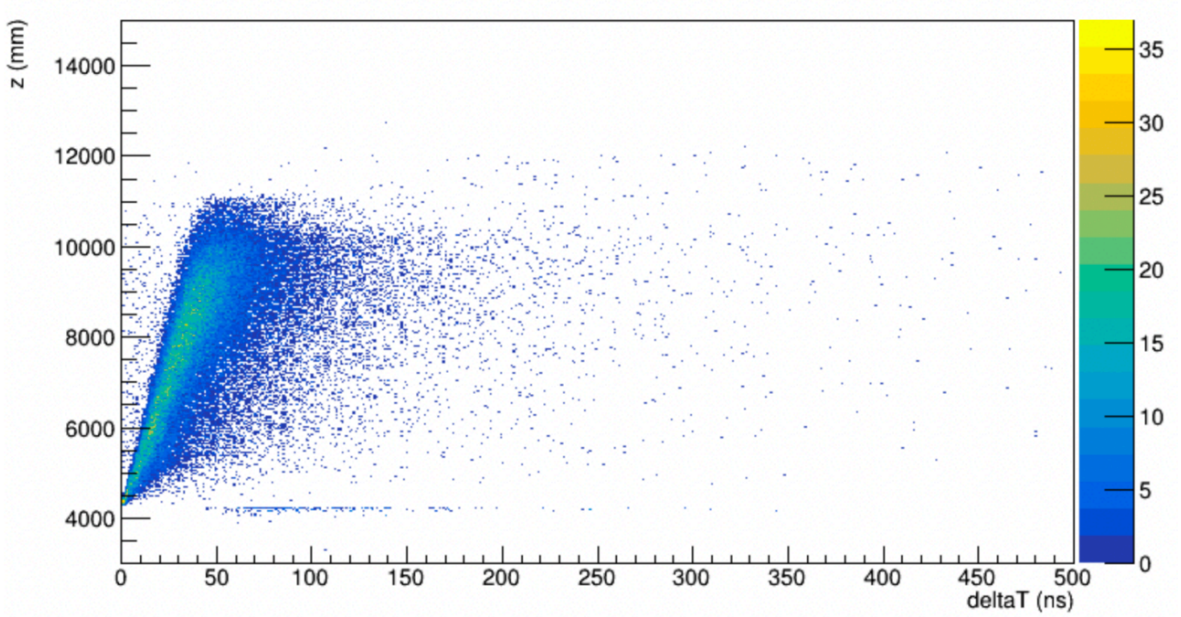

Figure 4.6. The muon decay position in Z versus the proper time difference in DS with normal muon lifetime. The distribution is produced from 10^{12} POT events.

In summary, the efficiencies of signal and backgrounds simulations are improved by the following methods:

- By turning off the pion decay in the simulation of stopped pions in the stopping target and degrader, the efficiency of simulation is improved by a factor of ~ 100. Combining with the resampling in the DS, the signal and backgrounds arising from stopped π^+ decays are simulated at the level of $O(10^{13}) - O(10^{15})$ protons-on-target (POT).

- By restricting the muon proper time between 0-150 ns in the DS, the efficiency of μ-DIF simulation is improved by a factor of ~ 15. Combining with the resampling in the TS and DS, the μ-DIF background is simulated at the level of $O(10^{13})$ protons-on-target (POT).

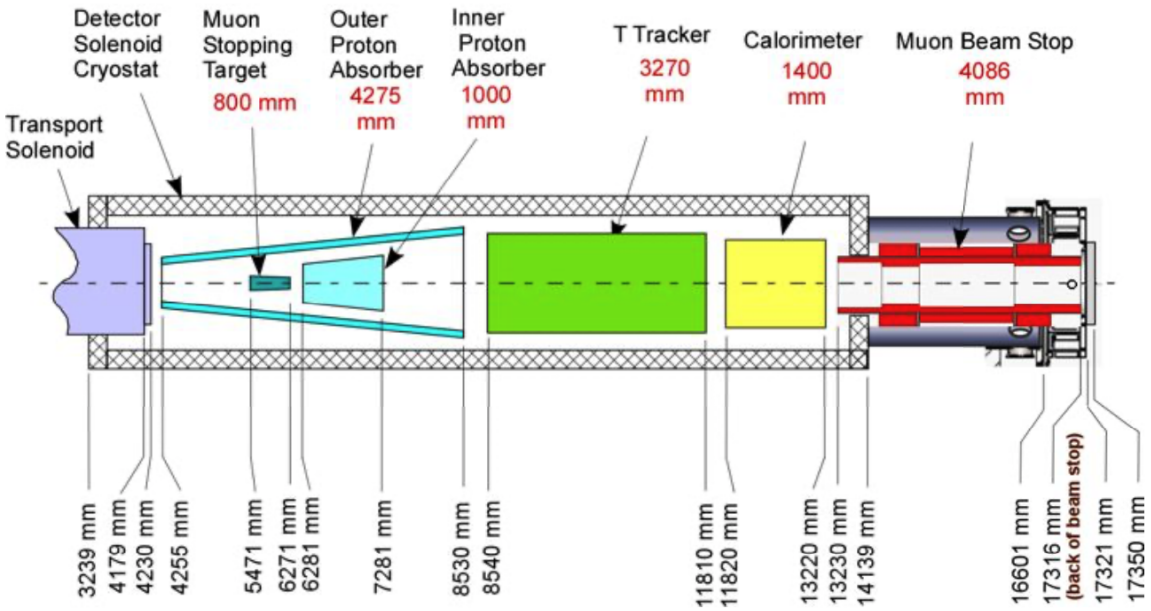

Figure 4.7. The Z position of the objects in Detector Solenoid using Mu2e coordinates.

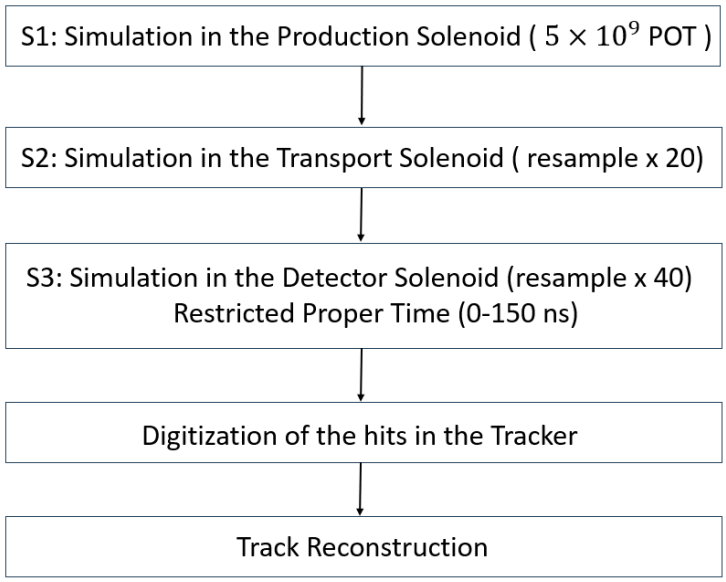

Figure 4.8. The diagram for the simulation of muon DIF background with restricted muon proper time between 0-150 ns.

5. SIGNAL AND BACKGROUNDS

The signal and backgrounds with different degrader thickness are simulated, using the toolkit and techniques described in the last chapter.

To illustrate the necessity of degrader, we first simulated the π^+ stops distributions in the stopping target without the degrader and with different degrader thickness, as shown in Figure 5.1. The π^+ stops distributions are produced from 10^8 POT.

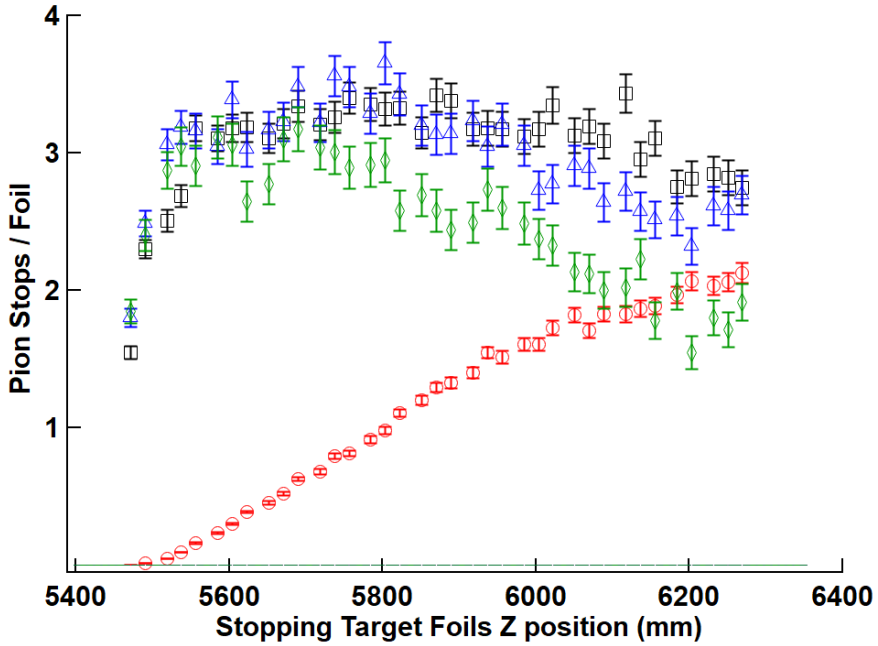

Figure 5.1. The π^+ stops distributions in the stopping target without degrader (Red Circle) and with 2 mm (Black Square), 3 mm (Blue Triangle), 4 mm (Green Rhombus) titanium degrader.

The π^+ stops rates for different degrader thickness are: 4.26×10^{-7} /POT (without the degrader), 1.13×10^{-6} /POT (2 mm Ti degrader), 1.10×10^{-6} /POT (3 mm Ti degrader), and 9.23×10^{-7} /POT (4 mm Ti degrader). Figure 5.1 shows that the existence of degrader can improve the π^+ stops rate in the stopping target and the rate is maximized with the 2 mm Ti degrader. We further optimized the Ti degrader thickness by the pion stops efficiency to muon flux efficiency ratio, as shown in Figure 3.7. The 4 mm Ti degrader makes the largest ratio at ~ 1.55, which reduces the μ flux by a factor of ~ 2 (in Figure 3.6) at the cost of 18% pion stops loss compared to 2mm Ti degrader. The 3 mm Ti degrader (second

optimized) reduces 25% μ flux compared to the 2 mm Ti degrader (in Figure 3.6), while makes almost same π^+ stops rate as the 2 mm Ti degrader. The simulation results of signal and backgrounds with 3mm and 4mm Ti degrader are presented in this chapter.

5.1 Stopped $\pi^+ \to e^+$ Signal

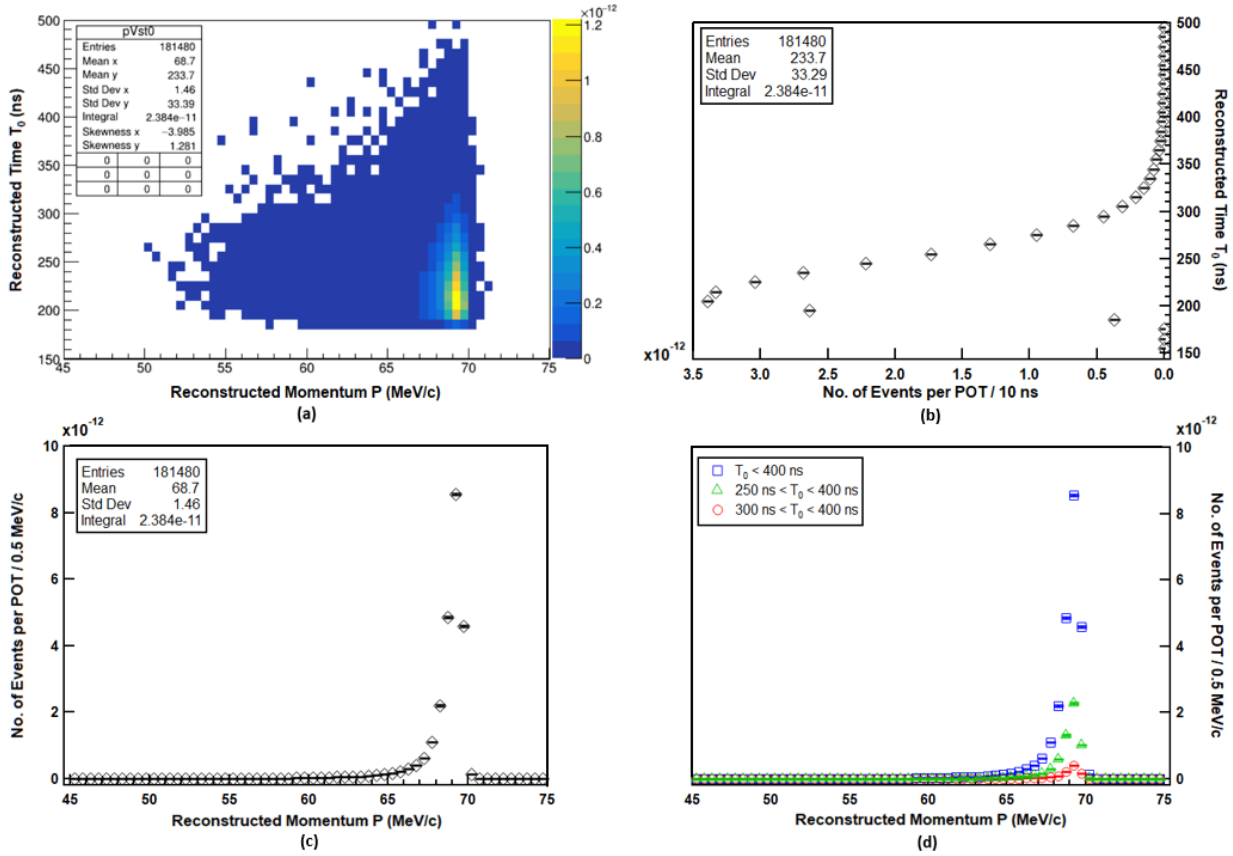

Figure 5.2. Stopped $\pi^+ \to e^+$ signal simulation with the 3mm Ti degrader: (a) Reconstructed Time versus Reconstructed Momentum. (b) Reconstructed Time distribution. (c) Reconstructed Momentum distribution. (d) Reconstructed Momentum distributions with cuts on the reconstructed time.

The simulation of stopped $\pi^+ \to e^+$ signal is carried out by the staged simulation, as shown in Figure 4.2. Figure 5.2 and Figure 5.3 show the time and momentum of reconstructed tracks with the 3mm and 4mm Ti degrader, respectively. All the reconstructed tracks are required to pass the pre-selection cuts listed in the last chapter. After being weighed and scaled properly, the plots in Figure 5.2 and Figure 5.3 are normalized to per Proton-on-Target

(POT). Figure 5.2(a) and Figure 5.3(a) show the reconstructed time versus reconstructed momentum, and give the signal yields: 2.38×10^{-11} /POT (3mm Ti degrader) and 1.76×10^{-11} /POT (4mm Ti degrader). The signal yield difference between 3mm and 4mm Ti degrader is mostly caused by the discrepancy in pion stops rates in the stopping target. The corresponding reconstructed time (Figure 5.2(b) and Figure 5.3(b)) and momentum distributions (Figure 5.2(c) and Figure 5.3(c)) have the peak at $\sim$ 200ns and $\sim$ 69 MeV/c. Figure 5.2(d) and Figure 5.3(d) show the momentum distributions of reconstructed tracks with different cuts on reconstructed time T_0. The long negative tail comes from radiative energy loss (Bremsstrahlung), while the core width comes mostly from straggling in the ionization energy loss. The high-side tail above 70 MeV/c is caused by the misreconstruction.

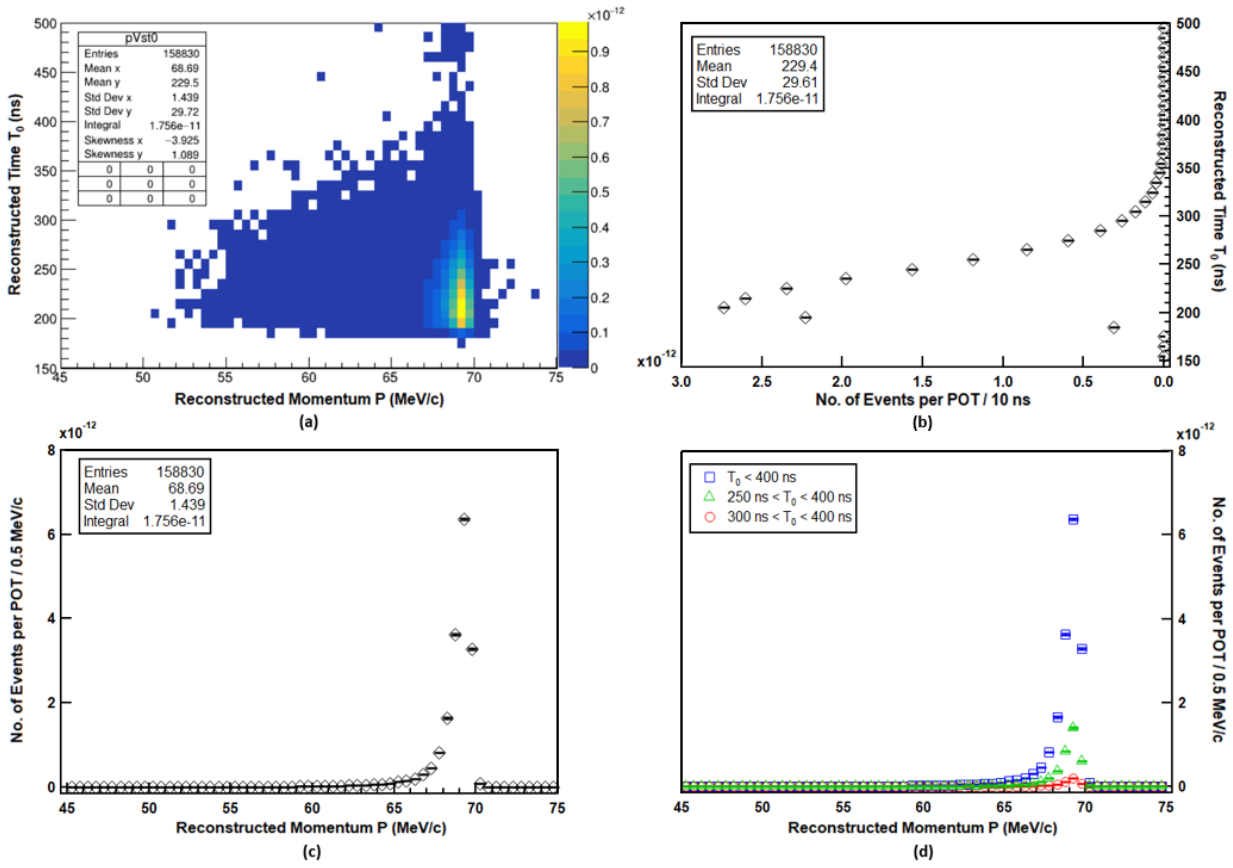

Figure 5.3. Stopped $\pi^+ \to e^+$ signal simulation with the 4mm Ti degrader: (a) Reconstructed Time versus Reconstructed Momentum. (b) Reconstructed Time distribution. (c) Reconstructed Momentum distribution. (d) Reconstructed Momentum distributions with cuts on the reconstructed time.

The signal yields (67.5-70.0 MeV/c) with different T_0 cuts and degrader thickness are listed in Table 5.1.

Table 5.1. Summary of the signal yields with different T_0 cuts and degrader thickness, normalized to protons-on-target (POT).

	$T_0 < 400$ ns	250 ns $< T_0 < 400$ ns	300 ns $< T_0 < 400$ ns
3 mm	$2.13 \times 10^{-11} \pm (5.73 \times 10^{-14})$	$(5.49 \pm 0.03) \times 10^{-12}$	$(9.21 \pm 0.11) \times 10^{-13}$
4 mm	$1.57 \times 10^{-11} \pm (4.41 \times 10^{-14})$	$(3.38 \pm 0.02) \times 10^{-12}$	$(4.43 \pm 0.07) \times 10^{-13}$

5.2 Stopped $\pi^+ \to e^+$ in Degrader Background

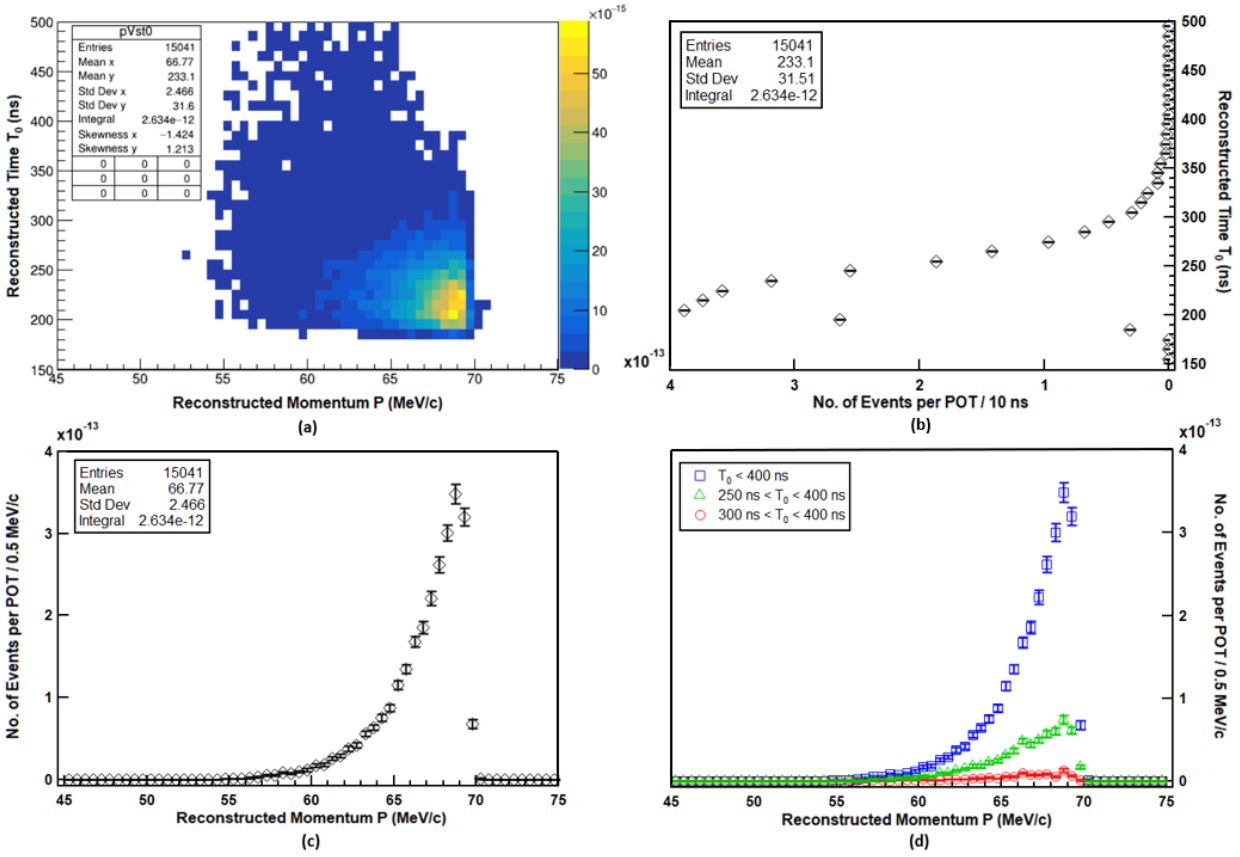

Figure 5.4. Stopped $\pi^+ \to e^+$ in degrader background simulation with the 3mm Ti degrader: (a) Reconstructed Time versus Reconstructed Momentum. (b) Reconstructed Time distribution.(c) Reconstructed Momentum distribution. (d) Reconstructed Momentum distributions with cuts on the reconstructed time.

The simulation of stopped $\pi^+ \to e^+$ in degrader background is carried out by the staged simulation in Figure 4.2. Figure 5.4 and Figure 5.5 show the time and momentum of reconstructed tracks with 3mm and 4mm Ti degrader, respectively. The reconstructed tracks are required to pass the pre-selection cuts and all plots are normalized to per Proton-on-Target (POT). The background yield of 4mm Ti degrader (3.11×10^{-12}/POT) is larger than that of 3mm Ti degrader (2.63×10^{-12}/POT), since there are more pion stops in thicker degrader. The different shapes of reconstructed momentum for 3mm and 4mm Ti degraders and the effects on signal peak shift will be discussed in the next chapter.

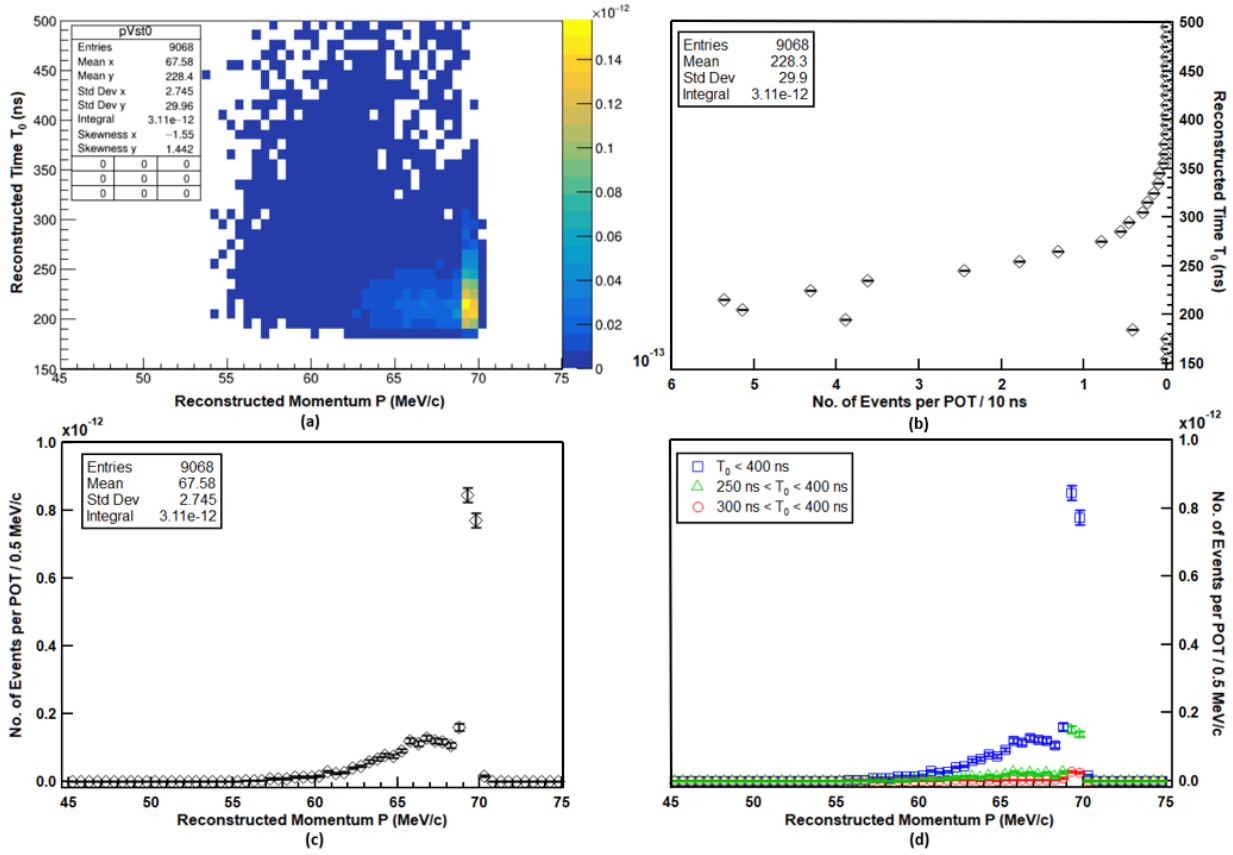

Figure 5.5. Stopped $\pi^+ \to e^+$ in degrader background simulation with the 4mm Ti degrader: (a) Reconstructed Time versus Reconstructed Momentum. (b) Reconstructed Time distribution.(c) Reconstructed Momentum distribution. (d) Reconstructed Momentum distributions with cuts on the reconstructed time.

The background yields (67.5-70.0 MeV/c) with different T_0 cuts and degrader thickness are listed in Table 5.2.

Table 5.2. Summary of the stopped $\pi^+ \to e^+$ in degrader background yields with different T_0 cuts and degrader thickness, normalized to protons-on-target (POT).

	$T_0 < 400$ ns	250 ns $< T_0 <$ 400 ns	300 ns $< T_0 <$ 400 ns
3 mm	$(1.30 \pm 0.02) \times 10^{-12}$	$(2.70 \pm 0.10) \times 10^{-13}$	$(3.42 \pm 0.33) \times 10^{-14}$
4 mm	$(2.00 \pm 0.03) \times 10^{-12}$	$(3.52 \pm 0.14) \times 10^{-13}$	$(6.38 \pm 0.60) \times 10^{-14}$

5.3 Stopped $\pi^+ \to \mu^+$ in Stopping Target Background

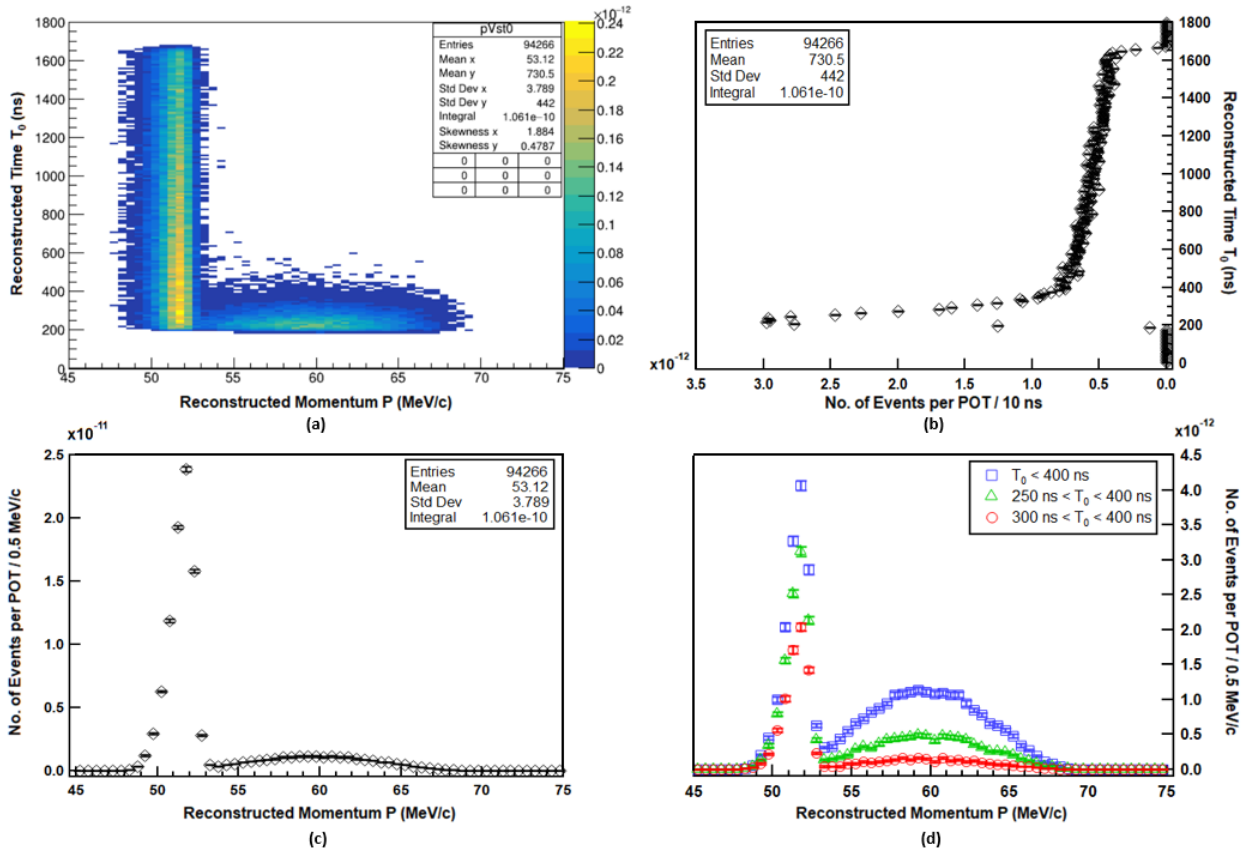

Figure 5.6. Stopped $\pi^+ \to \mu^+$ in stopping target background simulation with the 3mm Ti degrader: (a) Reconstructed Time versus Reconstructed Momentum. (b) Reconstructed Time distribution.(c) Reconstructed Momentum distribution. (d) Reconstructed Momentum distributions with cuts on the reconstructed time.

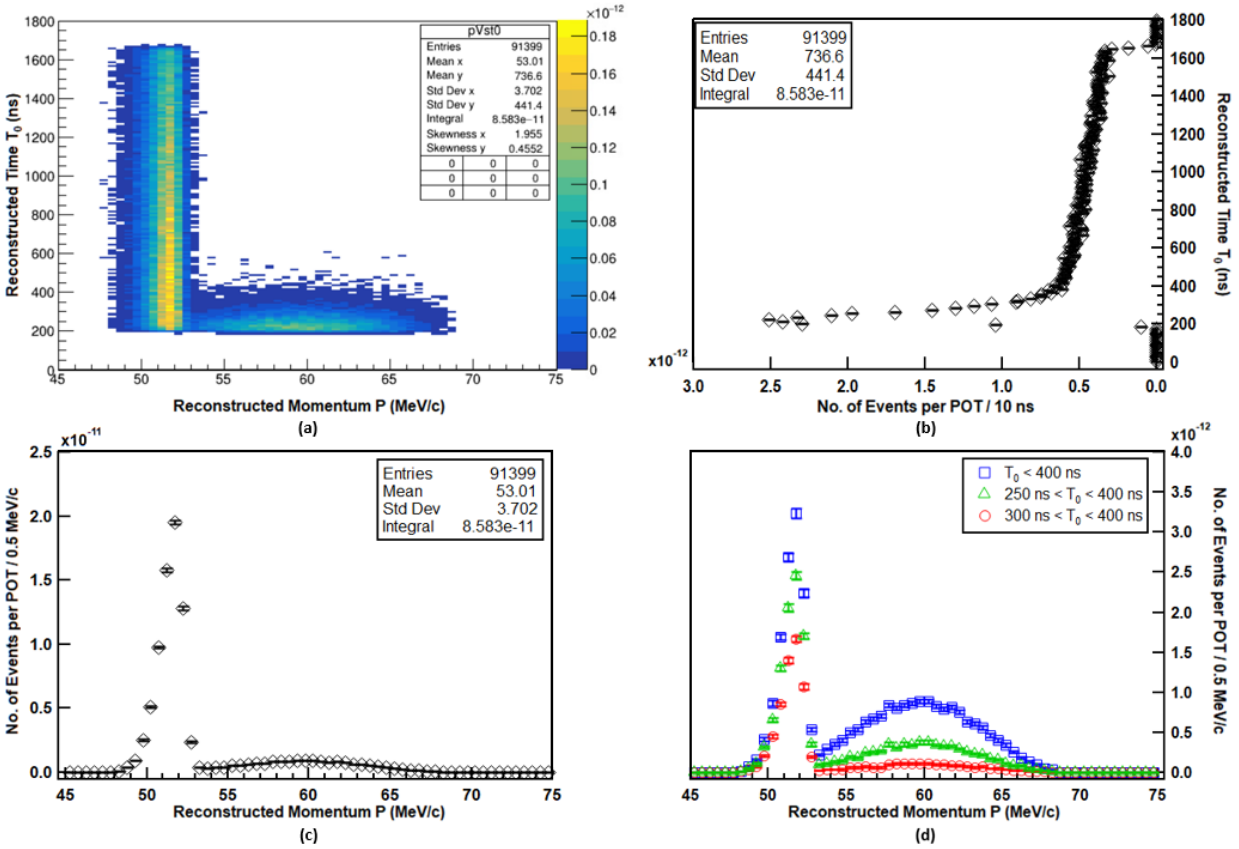

Figure 5.7. Stopped $\pi^+ \to \mu^+$ in stopping target background simulation with the 4mm Ti degrader: (a) Reconstructed Time versus Reconstructed Momentum. (b) Reconstructed Time distribution.(c) Reconstructed Momentum distribution. (d) Reconstructed Momentum distributions with cuts on the reconstructed time.

The simulation of stopped $\pi^+ \to \mu^+$ in stopping target background is carried out by the staged simulation in Figure 4.3. Figure 5.6 and Figure 5.7 show the time and momentum of reconstructed tracks with the 3mm and 4mm Ti degrader, respectively. The reconstructed tracks consist of two components:

- The Michel positrons: A Michel positron is a positron produced when a μ^+ decays at rest. In this case, the muons are stopped in the stopping target. The Michel positrons correspond to the peak (49-53 MeV/c) in the reconstructed momentum distribution. The high-side tail of the peak comes from the sharp cutoff of the Michel positron energy

spectrum at $\sim$ 52.8 MeV/c (approximately half of the muon mass), while the low-side tail is shaped by the momentum acceptance of the Tracker.

- Muons Decay-in-Flight to positrons: they correspond to the 53-70 MeV/c range in the reconstructed momentum distribution. The decay of stopped pions generate mono-energetic $\sim$ 30 MeV/c muons. Note that 30 MeV/c is the minimum momentum of the muon that can decay to a positron with momentum at $\sim$ 70 MeV/c, so the momentum distribution ends at $\sim$ 70 MeV/c.

The upper limit of the T_0 cut at 400ns can exclude the majority of Michel positrons. The background yields (67.5-70.0 MeV/c) with different T_0 cuts and degrader thickness are listed in Table 5.3.

Table 5.3. Summary of the stopped $\pi^+ \to \mu^+$ in stopping target background yields with different T_0 cuts and degrader thickness, normalized to protons-on-target (POT).

	$T_0 < 400$ ns	250 ns $< T_0 <$ 400 ns	300 ns $< T_0 <$ 400 ns
3 mm	$(1.35 \pm 0.14) \times 10^{-13}$	$(7.12 \pm 0.98) \times 10^{-14}$	$(2.79 \pm 0.59) \times 10^{-14}$
4 mm	$(8.86 \pm 0.97) \times 10^{-14}$	$(3.52 \pm 0.60) \times 10^{-14}$	$(1.28 \pm 0.37) \times 10^{-14}$

5.4 Stopped $\pi^+ \to \mu^+$ in Degrader Background

The simulation of stopped $\pi^+ \to \mu^+$ in degrader background is carried out by the staged simulation in Figure 4.3. Figure 5.8 and Figure 5.9 show the time and momentum of reconstructed tracks with the 3mm and 4mm Ti degrader, respectively. The reconstructed tracks also consist of two parts: the Michel positrons and muons Decay-in-Flight to positrons. The background yields (67.5-70.0 MeV/c) with different T_0 cuts and degrader thickness are:

Table 5.4. Summary of the stopped $\pi^+ \to \mu^+$ in degrader background yields with different T_0 cuts and degrader thickness, normalized to protons-on-target (POT).

	$T_0 < 400$ ns	250 ns $< T_0 <$ 400 ns	300 ns $< T_0 <$ 400 ns
3 mm	$< 2.5 \times 10^{-13}$	$< 2.6 \times 10^{-14}$	$< 3.9 \times 10^{-15}$
4 mm	$(3.98 \pm 1.36) \times 10^{-13}$	$(4.09 \pm 4.09) \times 10^{-14}$	$< 6.1 \times 10^{-15}$

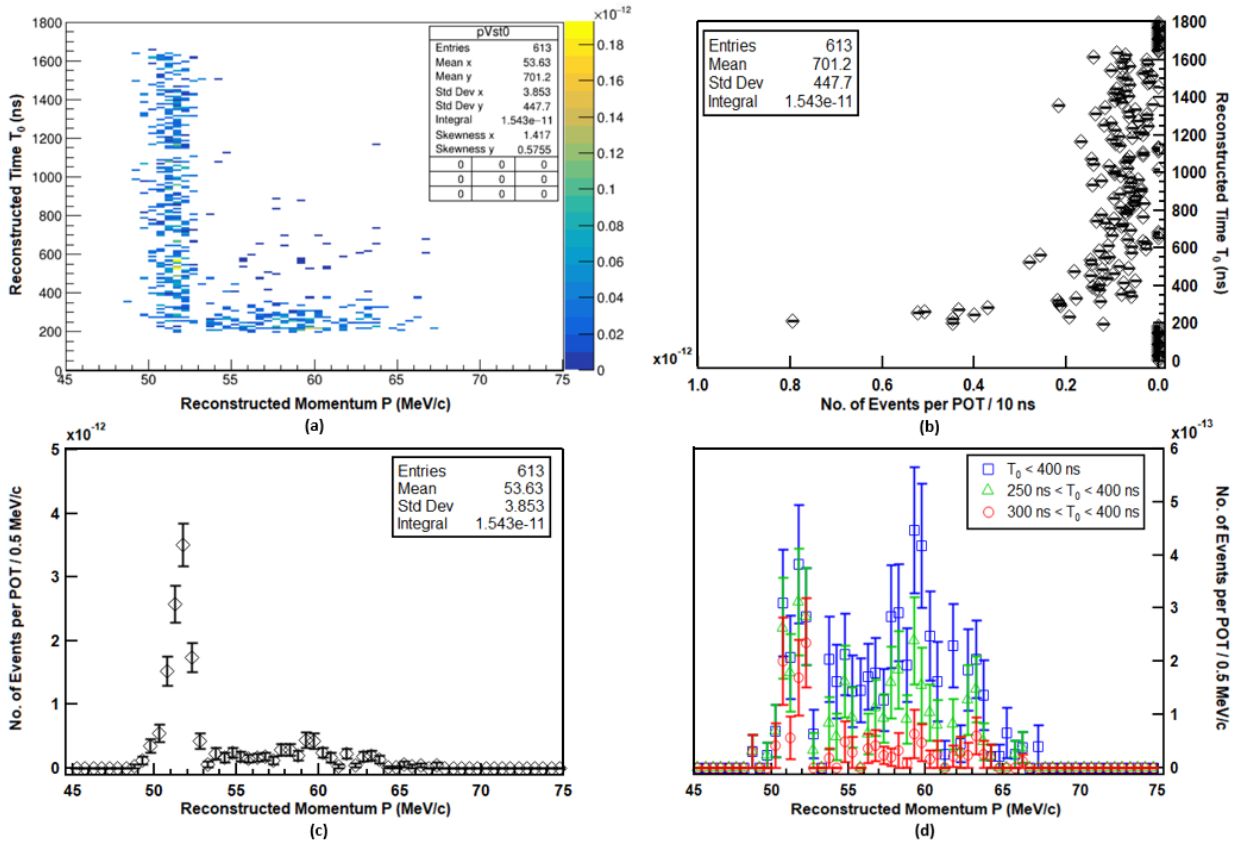

Figure 5.8. Stopped $\pi^+ \to \mu^+$ in degrader background simulation with the 3mm Ti degrader: (a) Reconstructed Time versus Reconstructed Momentum. (b) Reconstructed Time distribution.(c) Reconstructed Momentum distribution. (d) Reconstructed Momentum distributions with cuts on the reconstructed time.

5.5 Muon Decay-in-Flight Background

The μ-DIF background simulation is carried out by the staged simulation in Figure 4.8. Figure 5.10 and Figure 5.11 show the time and momentum of reconstructed tracks with the 3mm and 4mm Ti degrader, respectively. Figure 5.10 is produced from 1×10^{12} POT. Figure 5.11 is produced from 4×10^{12} POT. Both simulations restrict muon proper time between 0-150 ns in the detector solenoid. All plots are normalized to per POT.

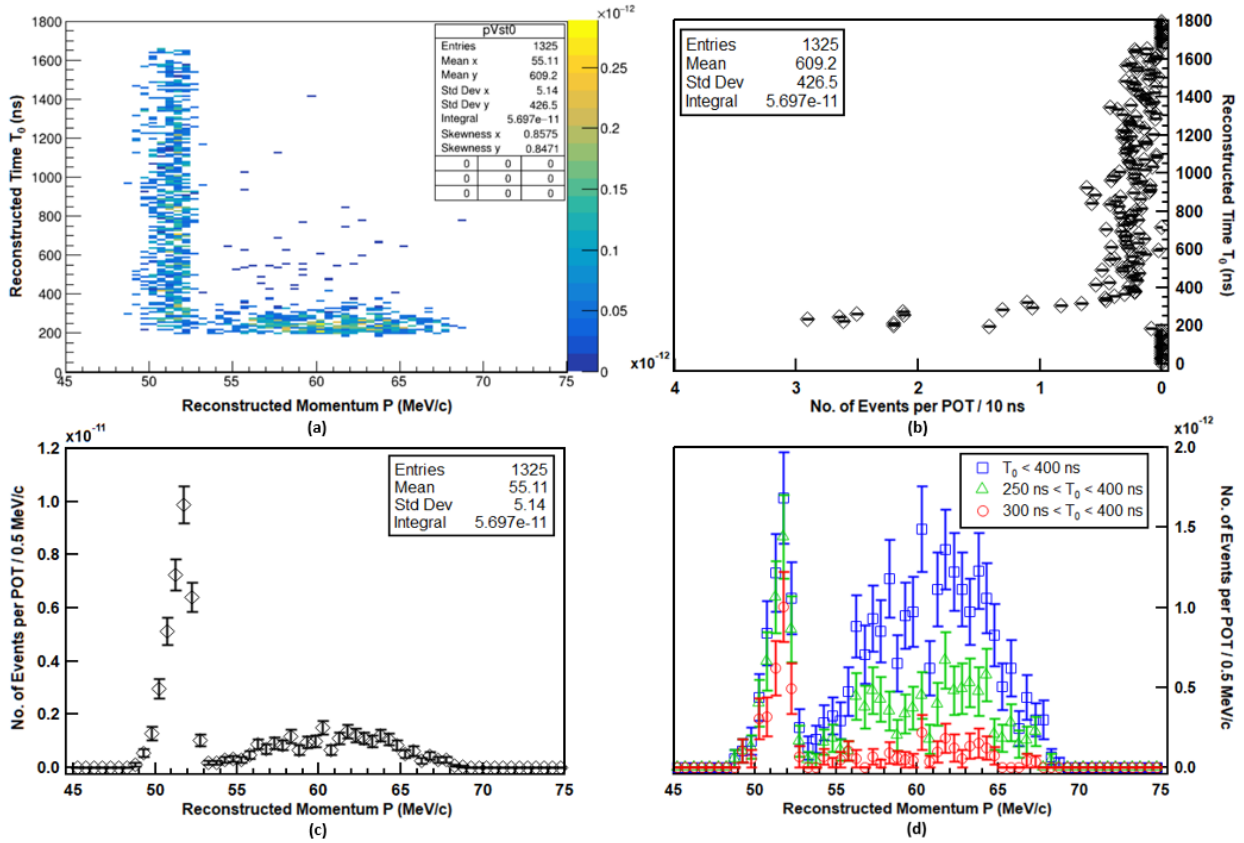

Figure 5.9. Stopped $\pi^+ \rightarrow \mu^+$ in degrader background simulation with the 4mm Ti degrader: (a) Reconstructed Time versus Reconstructed Momentum. (b) Reconstructed Time distribution.(c) Reconstructed Momentum distribution. (d) Reconstructed Momentum distributions with cuts on the reconstructed time.

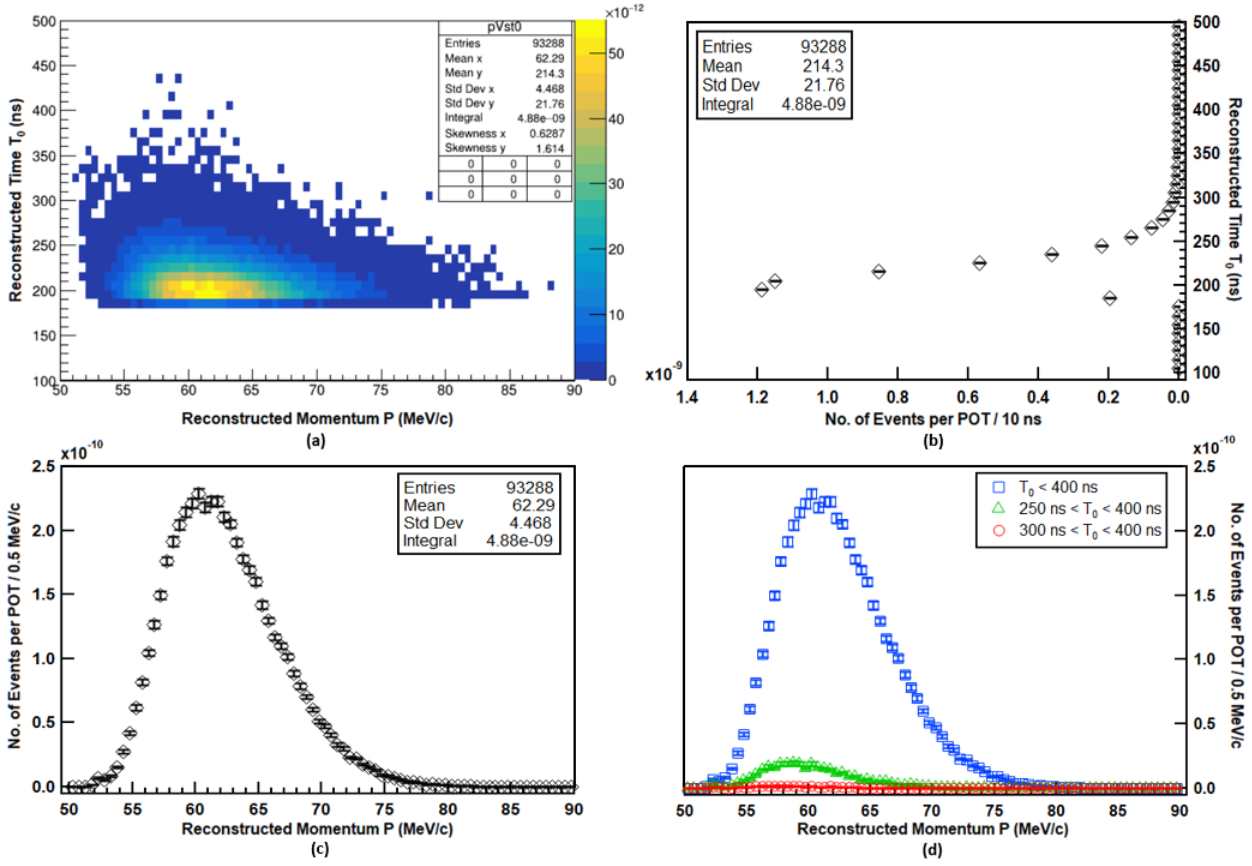

Figure 5.10. Muon DIF background simulation with the 3mm Ti degrader: (a) Reconstructed Time versus Reconstructed Momentum. (b) Reconstructed Time distribution.(c) Reconstructed Momentum distribution. (d) Reconstructed Momentum distributions with cuts on the reconstructed time.

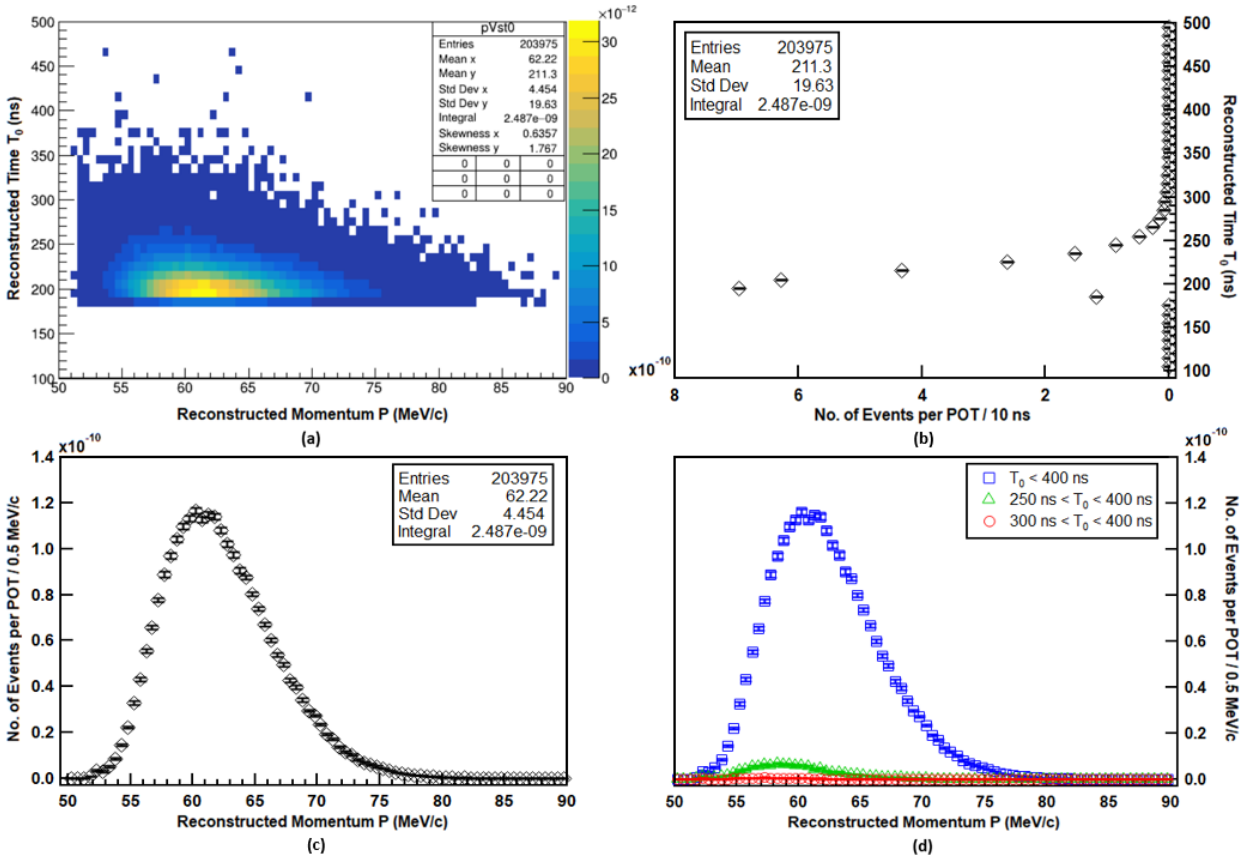

Figure 5.11. Muon DIF background simulation with the 4mm Ti degrader: (a) Reconstructed Time versus Reconstructed Momentum. (b) Reconstructed Time distribution.(c) Reconstructed Momentum distribution. (d) Reconstructed Momentum distributions with cuts on the reconstructed time.

The μ-DIF background yield with T_0 cut 300-400 ns will be underestimated if we use the integral as the yield directly, since there are some missing data points between 67.5-70 MeV/c, as shown in Figure 5.12. The yields are calculated from the integrals of the fits (red curves in Figure 5.12) of the μ-DIF background momentum distribution between 67.5-70 MeV/c. The fit function is given by:

$$f(x; A, \tau) = A \cdot \exp\left(\frac{-(x - x_0)}{\tau}\right), \quad x_0 = 60 \tag{5.1}$$

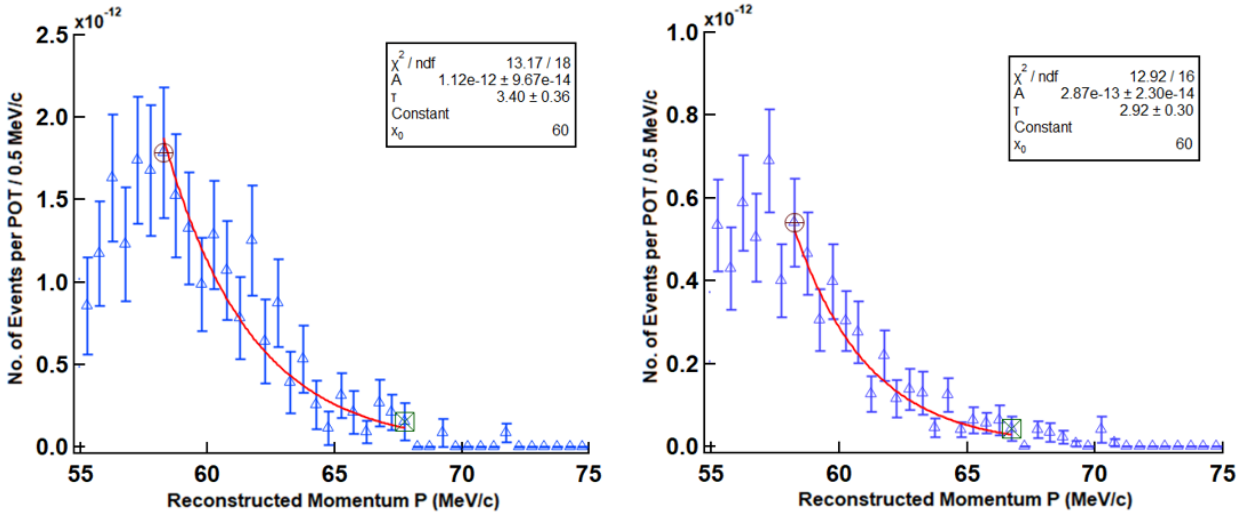

(a) (b)

Figure 5.12. (a) The reconstructed momentum of μ-DIF background with the 3mm Ti degrader and T_0 cut 300-400ns and its fit(red curve). (b) The reconstructed momentum of μ-DIF background with the 4mm Ti degrader and T_0 cut 300-400ns and its fit(red curve).

The background yields (67.5-70.0 MeV/c) with different T_0 cuts and degrader thickness are:

Table 5.5. Summary of the μ-DIF background yields with different T_0 cuts and degrader thickness, normalized to protons-on-target (POT).

	$T_0 < 400$ ns	250 ns $< T_0 < 400$ ns	300 ns $< T_0 < 400$ ns
3 mm	$(3.48 \pm 0.04) \times 10^{-10}$	$(1.07 \pm 0.08) \times 10^{-11}$	$(4.37 \pm 0.77) \times 10^{-13}$
4 mm	$(1.73 \pm 0.01) \times 10^{-10}$	$(2.74 \pm 0.19) \times 10^{-12}$	$(7.39 \pm 1.41) \times 10^{-14}$

The yields of signal and total background with different T_0 cuts and degrader thickness are summarized in Table 5.6. The T_0 cut 300-400 ns makes the largest S/B ratio for both degraders.

Table 5.6. Summary of the signal and total background yields with different T_0 cuts and degrader thickness, normalized to protons-on-target (POT).

3 mm	$T_0 < 400$ ns	250 ns $< T_0 < 400$ ns	300 ns $< T_0 < 400$ ns
Signal	2.13×10^{-11}	5.49×10^{-12}	9.21×10^{-13}
Total Background	3.49×10^{-10}	1.10×10^{-11}	4.99×10^{-13}
S/B ratio	0.06	0.50	1.85
4 mm	$T_0 < 400$ ns	250 ns $< T_0 < 400$ ns	300 ns $< T_0 < 400$ ns
Signal	1.57×10^{-11}	3.38×10^{-12}	4.43×10^{-13}
Total Background	1.75×10^{-10}	3.17×10^{-12}	1.51×10^{-13}
S/B ratio	0.09	1.07	2.93

The reconstructed momentum distributions of the stopped-π calibration signal and expected backgrounds with the 3mm and 4mm Ti degrader are shown in Figure 5.13 and Figure 5.14, respectively. All the reconstructed tracks are required to pass the pre-selection cuts and T_0 cut between 300-400 ns, where T_0 is the reconstructed time of track. From these distributions, the signal and background yields (67.5-70.0 MeV/c) are calculated, as shown in Table 5.7.

Table 5.7. Summary of the signal and background yields, normalized to protons-on-target (POT). The measurement uncertainties are statistical.

Signal	Yield (3mm)	Yield (4mm)
$\pi^+ \to e^+$ in Stopping Target	$(9.21 \pm 0.11) \times 10^{-13}$	$(4.43 \pm 0.07) \times 10^{-13}$
Background		
$\pi^+ \to e^+$ in Degrader	$(3.42 \pm 0.33) \times 10^{-14}$	$(6.38 \pm 0.60) \times 10^{-14}$
$\pi^+ \to \mu^+$ in Stopping Target	$(2.79 \pm 0.59) \times 10^{-14}$	$(1.28 \pm 0.37) \times 10^{-14}$
$\pi^+ \to \mu^+$ in Degrader	$< 3.9 \times 10^{-15}$	$< 6.1 \times 10^{-15}$
μ^+ Decay-In-Flight	$(4.37 \pm 0.77) \times 10^{-13}$	$(7.39 \pm 1.41) \times 10^{-14}$
Total	$(4.99 \pm 0.77) \times 10^{-13}$	$(1.51 \pm 0.16) \times 10^{-13}$
S/B ratio	1.85	2.93

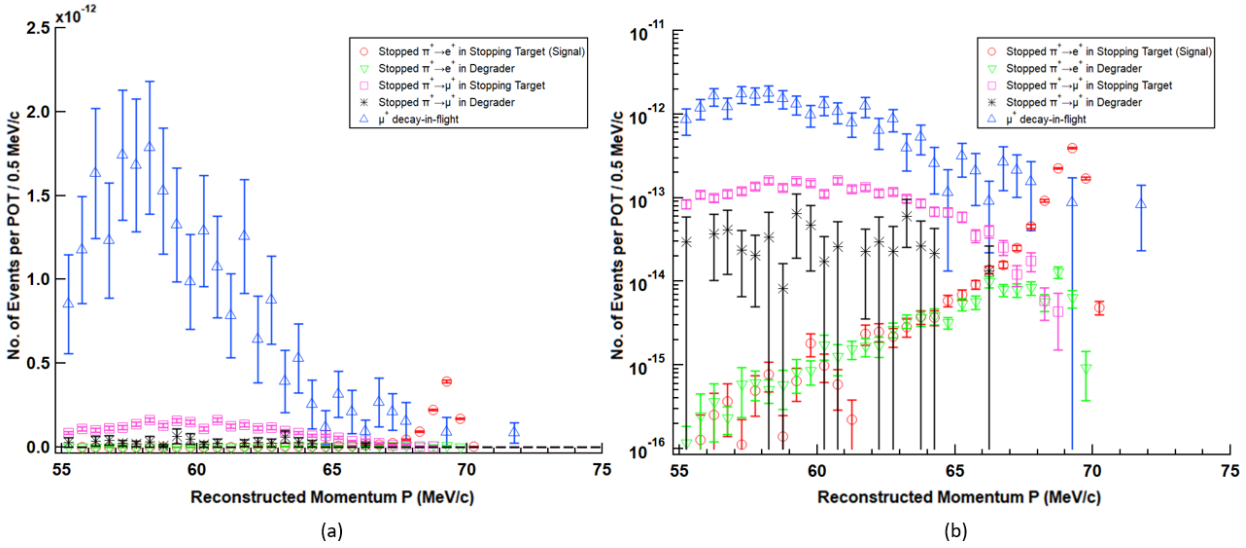

Figure 5.13. Resulting momentum distribution of the stopped-π calibration signal on top of expected backgrounds with the 3mm Ti degrader.(a) linear scale. (b) log scale. All the reconstructed tracks are required to pass the pre-selection cuts and T_0 cut between 300-400 ns.

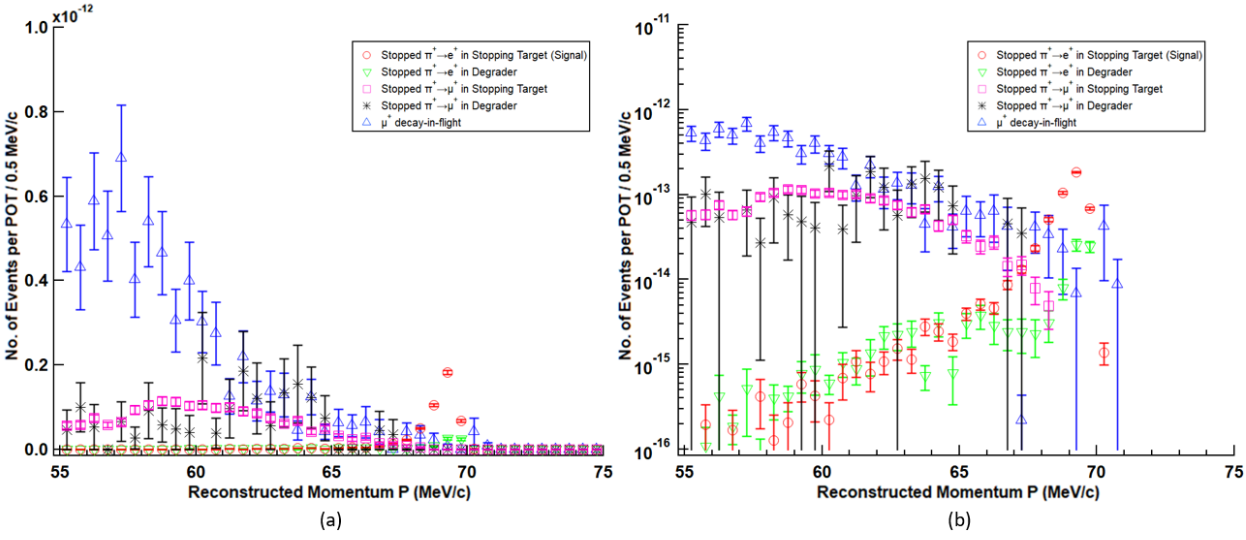

Figure 5.14. Resulting momentum distribution of the stopped-π calibration signal on top of expected backgrounds with the 4mm Ti degrader.(a) linear scale. (b) log scale. All the reconstructed tracks are required to pass the pre-selection cuts and T_0 cut between 300-400 ns.

6. FITTING AND PEAK SHIFT

The datasets of signal and backgrounds in Figure 5.13 and Figure 5.14 correspond to $O(10^{13}) - O(10^{15})$ protons-on-target (POT). The distributions in Figure 5.13 and Figure 5.14 are used for fitting the momentum spectra of signal and backgrounds, and studying the signal peak shift by backgrounds.

6.1 Signal Fitting

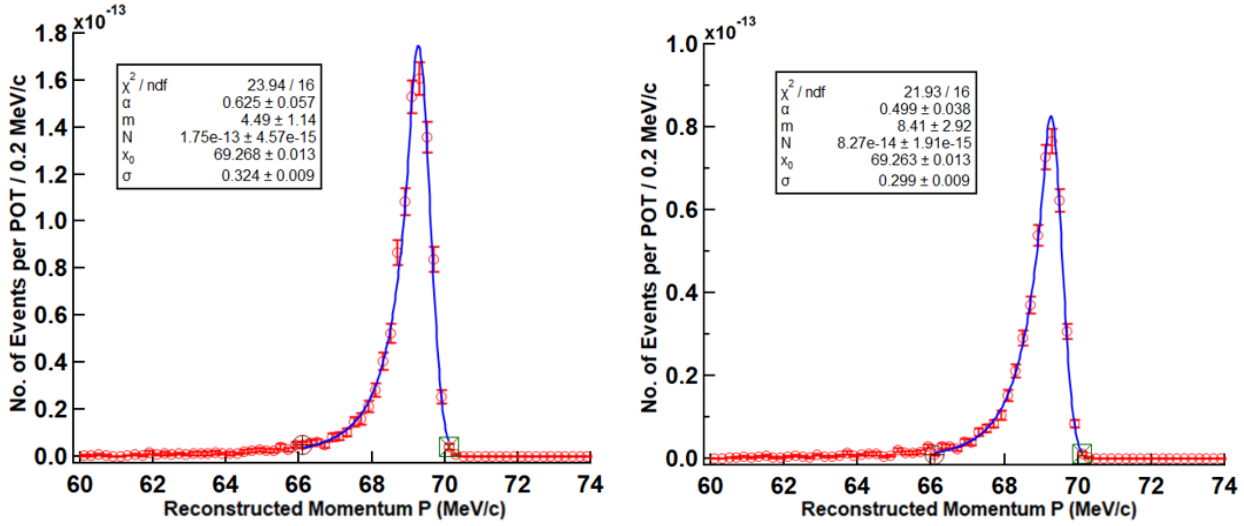

(a) (b)

Figure 6.1. (a) The reconstructed momentum distribution of signal (Red Circle) with the 3mm Ti degrader and its fit (Blue Curve). (b) The reconstructed momentum distribution of signal (Red Circle) with the 4mm Ti degrader and its fit (Blue Curve). All the reconstructed tracks are required to pass the preselection cuts and T_0 cut between 300-400 ns.

The parametrization of the signal e^+ reconstructed momentum, based on the crystal ball fit function is presented in Figure 6.1. The probability density function of crystal ball function is given by:

$$f(x;\alpha,m,x_0,\sigma,N) = N \cdot \begin{cases} \exp\left(-\frac{(x-x_0)^2}{2\sigma^2}\right), & \text{for } \frac{x-x_0}{\sigma} > -\alpha \\ A \cdot \left(B - \frac{x-x_0}{\sigma}\right)^{-m}, & \text{for } \frac{x-x_0}{\sigma} \leqslant -\alpha \end{cases} \tag{6.1}$$

where $A = (m/|\alpha|)^m \exp(-\alpha^2/2)$, $B = m/|\alpha| - |\alpha|$ and N is a scale factor. α defines the point where the pdf changes from a power-law to a Gaussian distribution. m is the power of the power-law tail. x_0 is the peak of the pdf.

The momentum distributions of signal in Figure 6.1 are plotted with 0.2 MeV/c bin size, to get more data points for fitting. For a test of significance at $\alpha = 0.05$ and df = 16, the χ^2 critical value is 26.30. It shows the reconstructed momentum distributions of the signal can be well fitted by the crystal ball function with the peak x_0 at 69.268 ± 0.013 MeV/c (with the 3mm Ti degrader) and 69.263 ± 0.013 MeV/c (with the 4mm Ti degrader).

6.2 Peak Shift by Stopped $\pi^+ \to e^+$ in Degrader Background

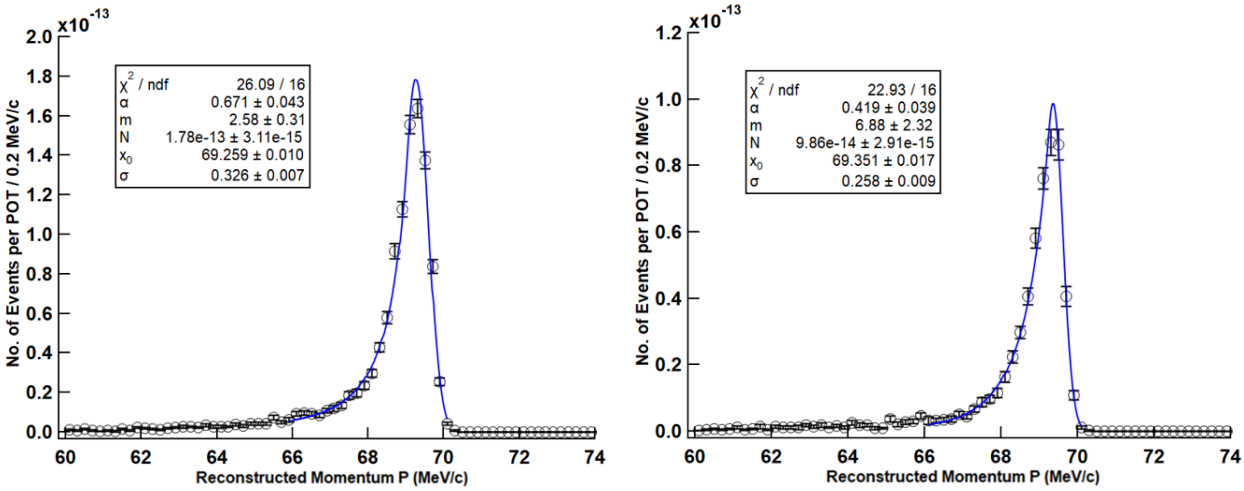

(a) (b)

Figure 6.2. (a) The reconstructed momentum distribution of the sum of signal and stopped $\pi^+ \to e^+$ in degrader background (Black Circle) with the 3mm Ti degrader and its fit (Blue Curve). (b) The reconstructed momentum distribution of the sum of signal and stopped $\pi^+ \to e^+$ in degrader background (Black Circle) with the 4mm Ti degrader and its fit (Blue Curve). All the reconstructed tracks are required to pass the pre-selection cuts and T_0 cut between 300-400 ns.

For the stopped $\pi^+ \to e^+$ in degrader background, its reconstructed momentum distribution has the similar shape as the signal. To study the peak shift by the background, we plot the the sum of signal and stopped $\pi^+ \to e^+$ in degrader background (Black Circle)

in Figure 6.2. The distributions are fitted by the crystal ball function with the peak x_0 at 69.259 ± 0.010 MeV/c (with the 3mm Ti degrader) and 69.351 ± 0.017 MeV/c (with the 4mm Ti degrader). The peak shifts caused by the stopped $\pi^+ \to e^+$ in degrader background are: -9 ± 16 keV/c (with the 3mm Ti degrader) and $+88 \pm 21$ keV/c (with the 4mm Ti degrader).

6.3 Peak Shift by Stopped $\pi^+ \to \mu^+$ in Stopping Target Background

Figure 6.3a and 6.3c show the reconstructed momentum of the stopped $\pi^+ \to \mu^+$ in stopping target background with the 3mm and 4mm Ti degrader, respectively. The momentum distributions are plotted with 0.5 MeV/c bin size and fitted by Gaussian function (54-66 MeV/c):

$$f(x; A, x_0, \sigma) = A \cdot \exp\left\{-\left(\frac{x - x_0}{\sigma}\right)^2\right\} \tag{6.2}$$

The error bars above 66 MeV/c are calculated from the values of parameters and their deviations:

$$\begin{aligned} \delta f = \tfrac{\delta A}{2.5} \cdot \exp\left\{-\left(\tfrac{x-x_0}{\sigma}\right)^2\right\} + \tfrac{A}{2.5} \cdot \exp\left\{-\left(\tfrac{x-x_0}{\sigma}\right)^2\right\} \tfrac{2(x-x_0)}{\sigma^2} \cdot \delta x_0 \\ + \tfrac{A}{2.5} \cdot \exp\left\{-\left(\tfrac{x-x_0}{\sigma}\right)^2\right\} \tfrac{2(x-x_0)^2}{\sigma^3} \cdot \delta\sigma \end{aligned} \tag{6.3}$$

The 2.5 is the scaling factor when the distribution is transformed from 0.5 MeV to 0.2 MeV bin size. Each term in the equation together with the error bars with the signal are added in quadrature, to get the corrected error bars in Figure 6.3b and 6.3d.

Figure 6.3b and 6.3d show the reconstructed momentum of signal with the error bars corrected by the background fit in the left with the 3mm and 4mm Ti degrader, respectively. The momentum distributions of signal with corrected error bars are fitted by the crystal ball function with the peak x_0 at 69.270 ± 0.015 MeV/c (with the 3mm Ti degrader) and 69.262 ± 0.014 MeV/c (with the 4mm Ti degrader). The peak shifts caused by the stopped $\pi^+ \to \mu^+$ in stopping target background are: $+2 \pm 20$ keV/c (with the 3mm Ti degrader) and -1 ± 19 keV/c (with the 4mm Ti degrader).

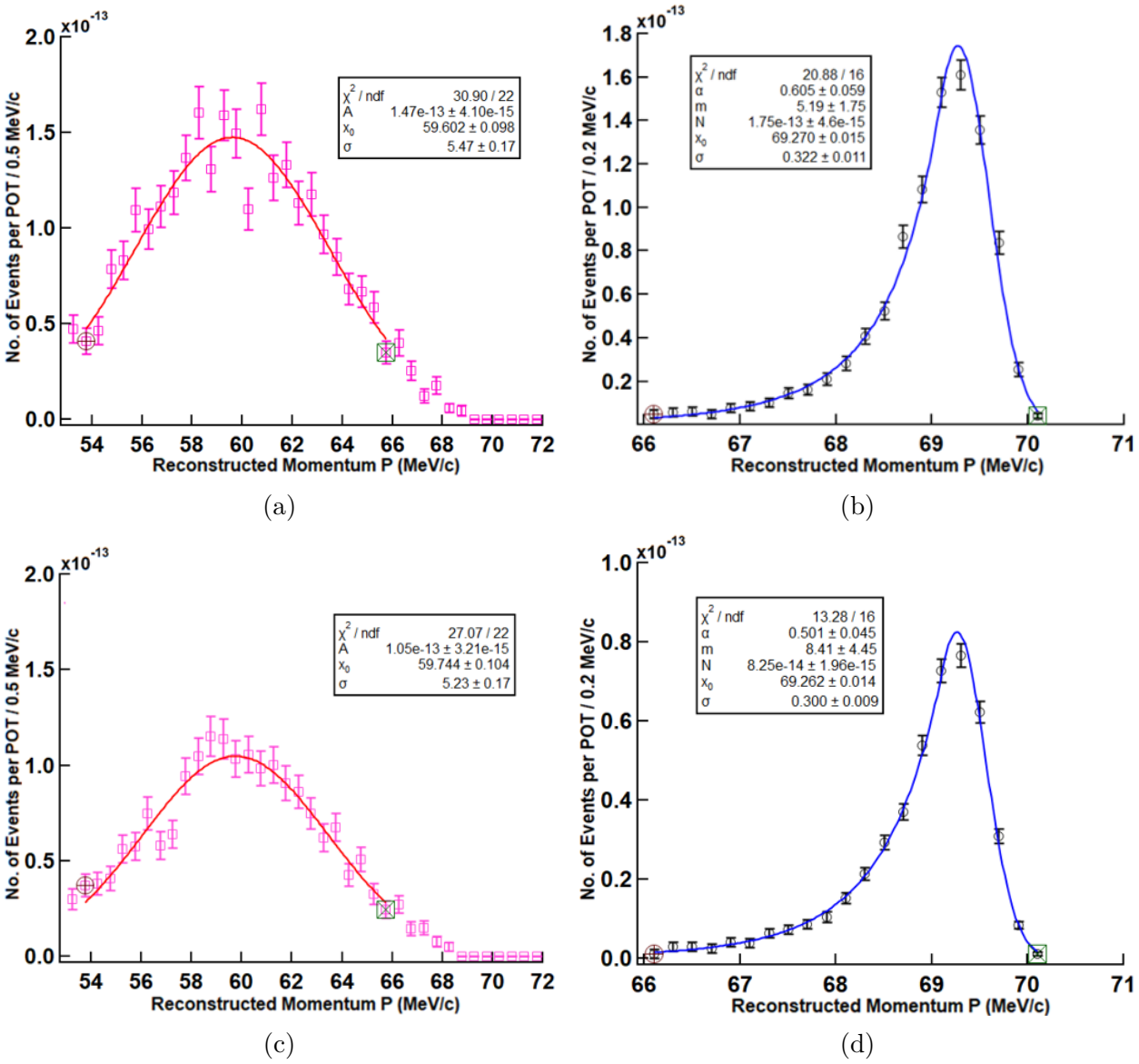

Figure 6.3. (a) The reconstructed momentum distribution of the stopped $\pi^+ \to \mu^+$ in stopping target background (Pink Square) with the 3mm Ti degrader and its fit (Red Curve). (b) The reconstructed momentum of signal (3mm Ti degrader) with the error bars corrected by the background fit in the left and its fit (Blue Curve). (c) The reconstructed momentum distribution of the stopped $\pi^+ \to \mu^+$ in stopping target background (Pink Square) with the 4mm Ti degrader and its fit (Red Curve). (d) The reconstructed momentum of signal (4mm Ti degrader) with the error bars corrected by the background fit in the left and its fit (Blue Curve). All the reconstructed tracks are required to pass the pre-selection cuts and T_0 cut between 300-400 ns.

6.4 Peak Shift by μ-DIF Background

Figure 6.4a and 6.4c show the reconstructed momentum of the μ-DIF background with the 3mm and 4mm Ti degrader, respectively. The momentum distributions are plotted with 0.5 MeV/c bin size and fitted by the exponential function:

$$f(x; A, \tau) = A \cdot \exp\left(\frac{-(x - x_0)}{\tau}\right), \quad x_0 = 60 \tag{6.4}$$

The errors above 66 MeV/c are calculated from the values of parameters and their deviations:

$$\delta f = \frac{\delta A}{2.5} \cdot \exp\left(\frac{-(x - x_0)}{\tau}\right) + \frac{A}{2.5} \cdot \exp\left(\frac{-(x - x_0)}{\tau}\right) \frac{x - x_0}{\tau^2} \delta\tau \tag{6.5}$$

The 2.5 is the scaling factor when the distribution is transformed from 0.5 MeV to 0.2 MeV bin size. Each term in the equation together with the error bars with the signal are added in quadrature, to get the corrected error bars in Figure 6.4b and 6.4d.

Figure 6.4b and 6.4d show the reconstructed momentum of signal with the error bars corrected by the background fit in the left with the 3mm and 4mm Ti degrader, respectively. The momentum distributions of signal with corrected error bars are fitted by the crystal ball function with the peak x_0 at 69.266 ± 0.032 MeV/c (with the 3mm Ti degrader) and 69.256 ± 0.017 MeV/c (with the 4mm Ti degrader). The peak shifts caused by the μ-DIF background are: -2 ± 34 keV/c (with the 3mm Ti degrader) and -7 ± 21 keV/c (with the 4mm Ti degrader).

The peak shifts caused by backgrounds are summarized in Table 6.1.

Table 6.1. Summary of the peak shifts caused by backgrounds.

Background	3mm	4mm
$\pi^+ \to e^+$ in Degrader	-9 ± 16 keV/c	$+88 \pm 21$ keV/c
$\pi^+ \to \mu^+$ in Stopping Target	$+2 \pm 20$ keV/c	-1 ± 19 keV/c
μ^+ Decay-In-Flight	-2 ± 34 keV/c	-7 ± 21 keV/c
Total	-9 ± 43 keV/c	$+80 \pm 35$ keV/c

The uncertainties in Table 6.1 are statistical. The datasets of signal and backgrounds correspond to $O(10^{13})$ protons-on-target (POT). The nominal Mu2e experiment runs with

4×10^7 protons/pulse and time interval of 1695 ns between pulses. To maintain the high efficiency of reconstruction algorithm, the beam intensity should be reduced to 1/50th of nominal. The $O(10^{13})$ POT datasets correspond to $O(1)$ min of data-taking. The statistical uncertainties are inversely proportional to $\sqrt{N_{POT}}$, that is $\sigma \sim 1/\sqrt{N_{POT}}$. Thus, the statistical uncertainties can be reduced to sub-keV level if we run the calibration with $O(1)$ week of data-taking.

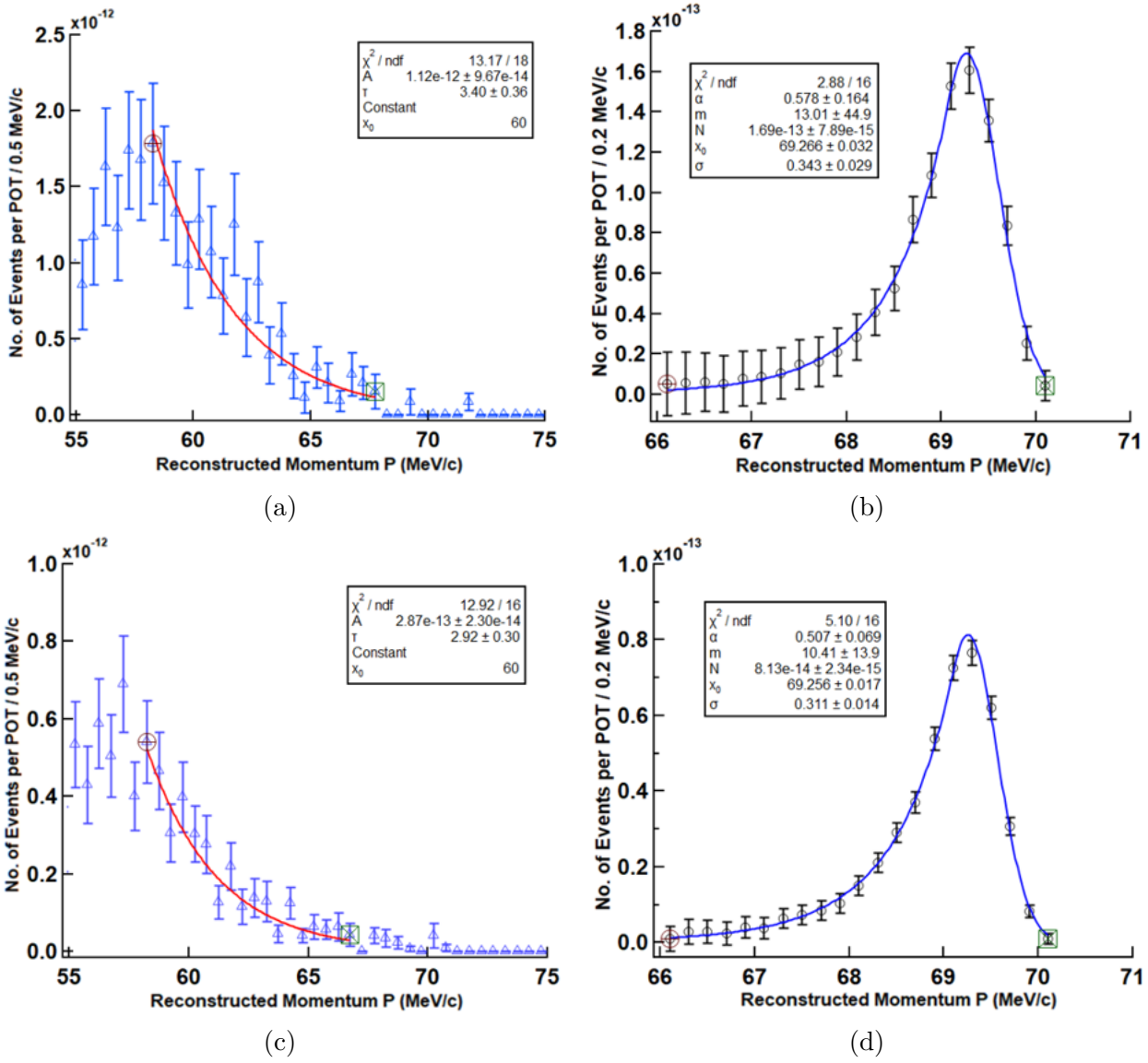

Figure 6.4. (a) The reconstructed momentum distribution of the μ-DIF background (Blue Triangle) with the 3mm Ti degrader and its fit (Red Curve). (b) The reconstructed momentum of signal (3mm Ti degrader) with the error bars corrected by the background fit in the left and its fit (Blue Curve). (c) The reconstructed momentum distribution of the μ-DIF background (Blue Triangle) with the 4mm Ti degrader and its fit (Red Curve). (d) The reconstructed momentum of signal (4mm Ti degrader) with the error bars corrected by the background fit in the left and its fit (Blue Curve). All the reconstructed tracks are required to pass the pre-selection cuts and T_0 cut between 300-400 ns.

7. SUMMARY

The 70 MeV/c positrons (e^+) from the decay of positively-charged pions (π^+) that have stopped in the aluminum stopping target are investigated as a calibration source to measure the absolute momentum scale and momentum resolution. The backgrounds for the calibration arise from μ^+ decay-in-flight (DIF) backgrounds and other stopped π^+ decays that produce reconstructed e^+ tracks mimicking a signal trajectory originating from the stopping target. The most significant background is the μ-DIF background. Therefore, we identified the need for a momentum degrader placed at the entry of the Detector Solenoid, to increase the pion stops in the stopping target and suppress the μ-DIF background. The material of the degrader is chosen to be titanium (Ti). The thickness of degrader is optimized by the pion stops efficiency to muon flux efficiency ratio (as shown in Figure 7.1) and the 4mm Ti degrader is the optimized one.

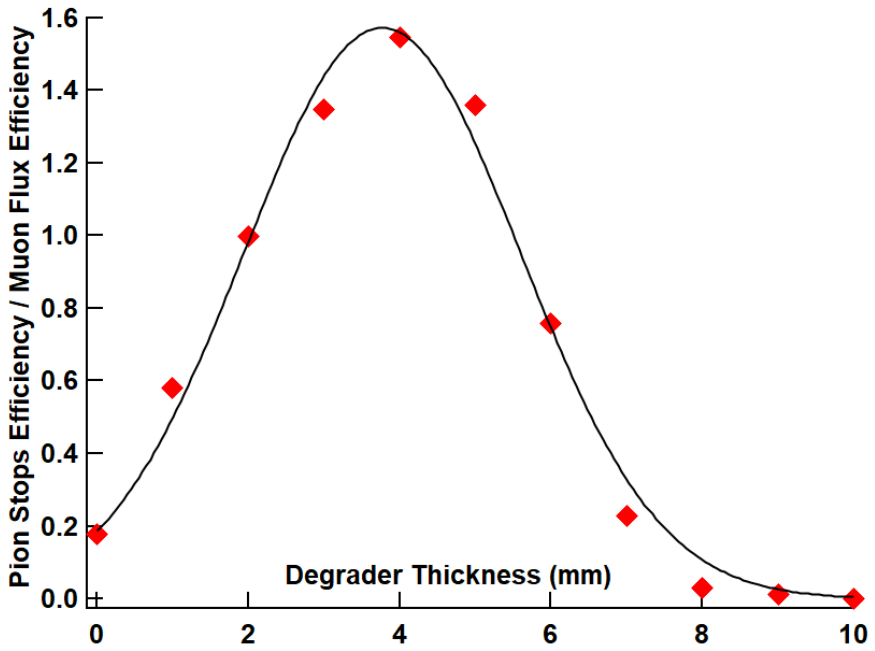

Figure 7.1. The pion stops efficiency to muon flux efficiency ratio as a function of degrader thickness.The black curve is given by Gaussian fitting.

Using the Mu2e Offline simulation framework, the expected signal and background processes and the Mu2e event reconstruction are simulated with the 3mm and 4mm Ti degrader

at the level of $O(10^{13})$ protons-on-target (POT). The resulting reconstructed momentum distributions of signal and backgrounds are presented in Figure 7.2. All the reconstructed tracks are required to pass the pre-selection cuts and T_0 (reconstructed time of track) cut between 300-400 ns. From these distributions, the signal and background yields between 67.5-70.0 MeV/c are calculated, as shown in Table 7.1.

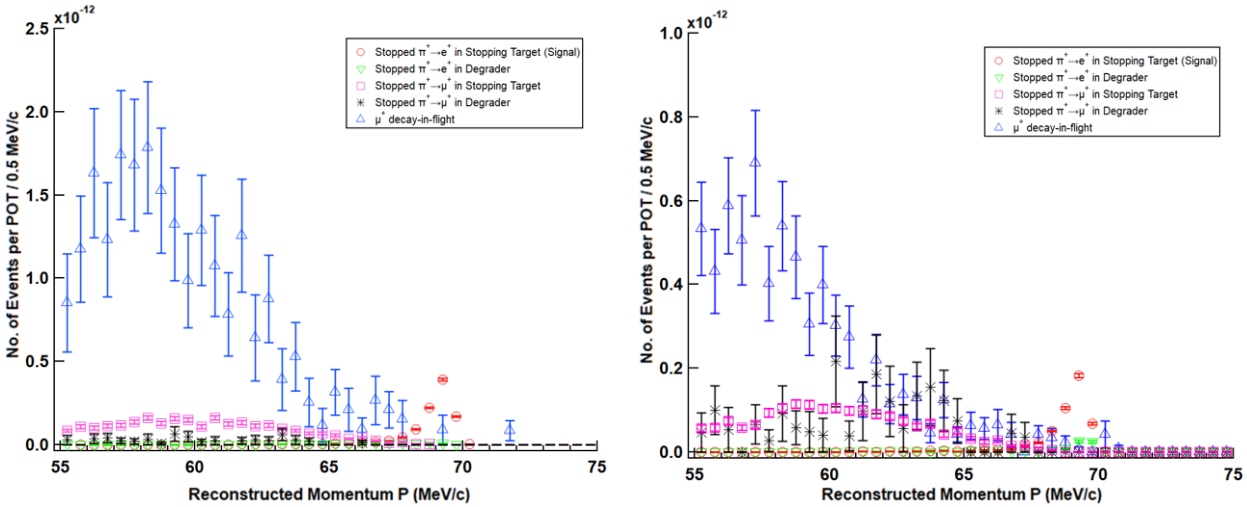

(a) (b)

Figure 7.2. Resulting momentum distribution of the stopped-π calibration signal on top of expected backgrounds.(a) 3mm Ti degrader. (b) 4mm Ti degrader.

Table 7.1. Summary of the signal and background yields, normalized to protons-on-target (POT). The measurement uncertainties are statistical.

	Yield (3mm)	Yield (4mm)
Signal	$(9.21 \pm 0.11) \times 10^{-13}$	$(4.43 \pm 0.07) \times 10^{-13}$
Total Background	$(4.99 \pm 0.77) \times 10^{-13}$	$(1.51 \pm 0.16) \times 10^{-13}$
S/B	1.85	2.93

The ratio of S/B is used as a figure of merit, as $B \gg 0$. The 4mm Ti degrader performs better than the 3mm Ti degrader in terms of the S/B ratio.

By fitting the reconstructed momentum distributions of signal (in Figure 7.2) using the crystal ball function, we extracted the signal distribution peak and width of $x_0 = 69.268 \pm$

0.013 MeV/c and $\sigma = 0.324 \pm 0.009$ MeV/c (with the 3mm Ti degrader), $x_0 = 69.263 \pm 0.013$ MeV/c and $\sigma = 0.299 \pm 0.009$ MeV/c (with the 4mm Ti degrader). The peak shifts caused by backgrounds are summarized in Table 7.2.

Table 7.2. Summary of the peak shifts caused by backgrounds. The uncertainties are statistical.

Background	3mm	4mm
$\pi^+ \to e^+$ in Degrader	-9 ± 16 keV/c	$+88 \pm 21$ keV/c
$\pi^+ \to \mu^+$ in Stopping Target	$+2 \pm 20$ keV/c	-1 ± 19 keV/c
μ^+ Decay-In-Flight	-2 ± 34 keV/c	-7 ± 21 keV/c
Total	-9 ± 43 keV/c	$+80 \pm 35$ keV/c

The statistical uncertainties in Table 7.2 can be reduced to sub-keV level if we run the calibration with $O(10^{17})$ POT, which corresponds $\sim$ 1 week run with 1/50th of nominal intensity. Figure 7.3 shows the momentum spectra of reconstructed events with the 3mm (Black) and 4mm (Red) Ti degrader when running the calibration with 3×10^{16} POT. The peak shifts by backgrounds for both degraders are within 100 keV/c momentum scale accuracy requirement.

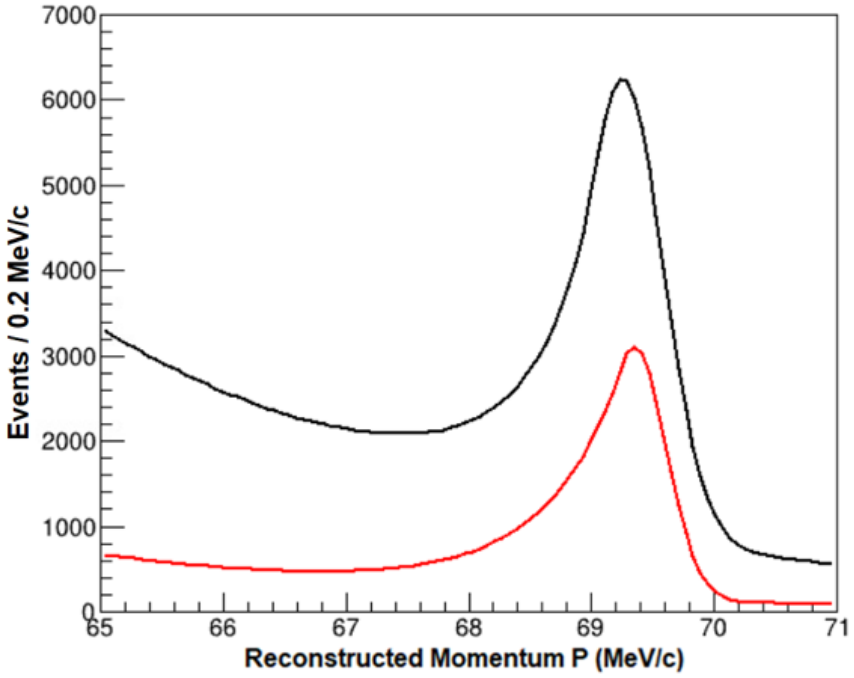

Figure 7.3. The momentum spectra of reconstructed events with the 3mm (Black) and 4mm (Red) Ti degrader when running the calibration with 3×10^{16} POT. There are 76394 reconstructed events for the 3mm Ti degrader, 24175 reconstructed events for the 4mm Ti degrader. All the reconstructed events are required to pass the pre-selection cuts and T_0 (reconstructed time of track) cut between 300-400 ns.

REFERENCES

[1] L. Bartoszek, E. Barnes, J. P. Miller, *et al.*, *Mu2e technical design report*, 2015. arXiv: 1501.05241 [physics.ins-det].

[2] M. Collaboration, *Mu2e run i sensitivity projections for the neutrinoless $\mu^- \to e^-$ conversion search in aluminum*, 2022. arXiv: 2210.11380 [hep-ex].

[3] J. Allison, K. Amako, J. Apostolakis, *et al.*, "Geant4 developments and applications," *IEEE Transactions on Nuclear Science*, vol. 53, no. 1, pp. 270–278, 2006. DOI: 10.1109/TNS.2006.869826.

[4] S. Agostinelli, J. Allison, K. Amako, *et al.*, "Geant4a simulation toolkit," *Nuclear Instruments and Methods in Physics Research Section A: Accelerators, Spectrometers, Detectors and Associated Equipment*, vol. 506, no. 3, pp. 250–303, 2003, ISSN: 0168-9002. DOI: https://doi.org/10.1016/S0168-9002(03)01368-8. [Online]. Available: https://www.sciencedirect.com/science/article/pii/S0168900203013688.

[5] J. Allison, K. Amako, J. Apostolakis, *et al.*, "Recent developments in geant4," *Nuclear Instruments and Methods in Physics Research Section A: Accelerators, Spectrometers, Detectors and Associated Equipment*, vol. 835, pp. 186–225, 2016, ISSN: 0168-9002. DOI: https://doi.org/10.1016/j.nima.2016.06.125. [Online]. Available: https://www.sciencedirect.com/science/article/pii/S0168900216306957.

[6] G. Isidori, Y. Nir, and G. Perez, "Flavor physics constraints for physics beyond the standard model," *Annual Review of Nuclear and Particle Science*, vol. 60, no. Volume 60, 2010, pp. 355–380, 2010, ISSN: 1545-4134. DOI: https://doi.org/10.1146/annurev.nucl.012809.104534. [Online]. Available: https://www.annualreviews.org/content/journals/10.1146/annurev.nucl.012809.104534.

[7] *La Rivista del Nuovo Cimento*, vol. 41, no. 2, pp. 71–174, Jan. 2018, ISSN: 0393697X, 0393697X. DOI: 10.1393/ncr/i2018-10144-0. [Online]. Available: https://doi.org/10.1393/ncr/i2018-10144-0.

[8] M. Raidal, A. van der Schaaf, I. Bigi, *et al.*, "Flavor physics of leptons and dipole moments," *The European Physical Journal C*, vol. 57, no. 12, pp. 13–182, Sep. 2008, ISSN: 1434-6052. DOI: 10.1140/epjc/s10052-008-0715-2. [Online]. Available: http://dx.doi.org/10.1140/epjc/s10052-008-0715-2.

[9] A. de Gouvêa and P. Vogel, "Lepton flavor and number conservation, and physics beyond the standard model," *Progress in Particle and Nuclear Physics*, vol. 71, pp. 75–92, Jul. 2013, ISSN: 0146-6410. DOI: 10.1016/j.ppnp.2013.03.006. [Online]. Available: http://dx.doi.org/10.1016/j.ppnp.2013.03.006.

[10] Y. Kuno and Y. Okada, "Muon decay and physics beyond the standard model," *Reviews of Modern Physics*, vol. 73, no. 1, pp. 151–202, Jan. 2001, ISSN: 1539-0756. DOI: 10.1103/revmodphys.73.151. [Online]. Available: http://dx.doi.org/10.1103/RevModPhys.73.151.

[11] A. Czarnecki, W. J. Marciano, and K. Melnikov, "Coherent muon-electron conversion in muonic atoms," in *The workshop on physics at the first muon collider and at the front end of a muon collider*, ASCE, 1998. DOI: 10.1063/1.56214. [Online]. Available: http://dx.doi.org/10.1063/1.56214.

[12] R. Bernstein and P. S. Cooper, "Charged lepton flavor violation: An experimenters guide," *Physics Reports*, vol. 532, no. 2, pp. 27–64, Nov. 2013, ISSN: 0370-1573. DOI: 10.1016/j.physrep.2013.07.002. [Online]. Available: http://dx.doi.org/10.1016/j.physrep.2013.07.002.

[13] L. Calibbi and G. Signorelli, "Charged lepton flavour violation: An experimental and theoretical introduction," *Rivista Del Nuovo Cimento*, vol. 41, p. 1, 2017.

[14] M. Raidal, A. Van der Schaaf, I. Bigi, *et al.*, "Flavor physics of leptons and dipole moments," *The European Physical Journal C*, vol. 57, pp. 13–182, 2008.

[15] T. M. Collaboration, *Search for the lepton flavour violating decay $\mu^+ \to e^+\gamma$ with the full dataset of the meg experiment*, 2016. arXiv: 1605.05081 [hep-ex].

[16] A. Baldini, Y. Bao, E. Baracchini, *et al.*, "Search for the lepton flavour violating decay $\mu \to e^+\gamma$ with the full dataset of the meg experiment," *European Physical Journal C*, vol. 76, May 2016.

[17] W. H. Bertl *et al.*, "Search for the Decay $\mu^+ \to e^+e^+e^-$," *Nucl. Phys. B*, vol. 260, pp. 1–31, 1985. DOI: 10.1016/0550-3213(85)90308-6.

[18] W. H. Bertl *et al.*, "A Search for muon to electron conversion in muonic gold," *Eur. Phys. J. C*, vol. 47, pp. 337–346, 2006. DOI: 10.1140/epjc/s2006-02582-x.

[19] A. M. Baldini, E. Baracchini, C. Bemporad, *et al.*, "The design of the meg ii experiment," *The European Physical Journal C*, vol. 78, no. 5, May 2018, ISSN: 1434-6052. DOI: 10.1140/epjc/s10052-018-5845-6. [Online]. Available: http://dx.doi.org/10.1140/epjc/s10052-018-5845-6.

[20] N. Berger, "The mu3e experiment," *Nuclear Physics B - Proceedings Supplements*, vol. 248-250, pp. 35–40, 2014, 1st Conference on Charged Lepton Flavor Violation, ISSN: 0920-5632. DOI: https://doi.org/10.1016/j.nuclphysbps.2014.02.007. [Online]. Available: https://www.sciencedirect.com/science/article/pii/S0920563214000085.

[21] Papa, Angela, "Charged lepton flavour violation searches at the paul scherrer institut: Status of the megii and mu3e experiments," *EPJ Web Conf.*, vol. 179, p. 01 018, 2018. DOI: 10.1051/epjconf/201817901018. [Online]. Available: https://doi.org/10.1051/epjconf/201817901018.

[22] C. Wu, "Search for muon to electron conversion at j-parc: The comet experiment," *Nuclear and Particle Physics Proceedings*, vol. 287-288, pp. 173–176, 2017, The 14th International Workshop on Tau Lepton Physics, ISSN: 2405-6014. DOI: https://doi.org/10.1016/j.nuclphysbps.2017.03.070. [Online]. Available: https://www.sciencedirect.com/science/article/pii/S2405601417301396.

[23] B. Aubert, Y. Karyotakis, J. P. Lees, *et al.*, "Searches for lepton flavor violation in the decays $\tau^{\pm} \to e^{\pm}\gamma$ and $\tau^{\pm} \to \mu^{\pm}\gamma$," *Phys. Rev. Lett.*, vol. 104, p. 021 802, 2 Jan. 2010. DOI: 10.1103/PhysRevLett.104.021802. [Online]. Available: https://link.aps.org/doi/10.1103/PhysRevLett.104.021802.

[24] K. Hayasaka, K. Inami, Y. Miyazaki, *et al.*, "Search for lepton-flavor-violating decays into three leptons with 719 million produced tau+tau- pairs," *Physics Letters B*, vol. 687, no. 23, pp. 139–143, Apr. 2010, ISSN: 0370-2693. DOI: 10.1016/j.physletb.2010.03.037. [Online]. Available: http://dx.doi.org/10.1016/j.physletb.2010.03.037.

[25] R. Aaij, B. Adeva, M. Adinolfi, *et al.*, "Search for the lepton-flavor-violating decays $B_s^0 \to e^{\pm}\mu^{\mp}$ and $B^0 \to e^{\pm}\mu^{\mp}$," *Phys. Rev. Lett.*, vol. 111, p. 141 801, 14 Sep. 2013. DOI: 10.1103/PhysRevLett.111.141801. [Online]. Available: https://link.aps.org/doi/10.1103/PhysRevLett.111.141801.

[26] R. Aaij, C. Abellán Beteta, T. Ackernley, *et al.*, "Search for lepton-flavor violating decays $B^+ \to K^+\mu^{\pm}e^{\mp}$," *Phys. Rev. Lett.*, vol. 123, p. 241 802, 24 Dec. 2019. DOI: 10.1103/PhysRevLett.123.241802. [Online]. Available: https://link.aps.org/doi/10.1103/PhysRevLett.123.241802.

[27] D. Ambrose, C. Arroyo, M. Bachman, *et al.*, "New limit on muon and electron lepton number violation from $K_L^0 \to \mu^{\pm} e^{\mp}$ decay," *Phys. Rev. Lett.*, vol. 81, pp. 5734–5737, 26 Dec. 1998. DOI: 10.1103/PhysRevLett.81.5734. [Online]. Available: https://link.aps.org/doi/10.1103/PhysRevLett.81.5734.

[28] A. Sher, R. Appel, G. S. Atoyan, *et al.*, "Improved upper limit on the decay $K^+ \to \pi^+ \mu^+ e^-$," *Phys. Rev. D*, vol. 72, p. 012 005, 1 Jul. 2005. DOI: 10.1103/PhysRevD.72.012005. [Online]. Available: https://link.aps.org/doi/10.1103/PhysRevD.72.012005.

[29] A. de Gouvêa and P. Vogel, "Lepton flavor and number conservation, and physics beyond the standard model," *Progress in Particle and Nuclear Physics*, vol. 71, pp. 75–92, 2013, Fundamental Symmetries in the Era of the LHC, ISSN: 0146-6410. DOI: https://doi.org/10.1016/j.ppnp.2013.03.006. [Online]. Available: https://www.sciencedirect.com/science/article/pii/S0146641013000252.

[30] A. Czarnecki, X. Garcia i Tormo, and W. J. Marciano, "Muon decay in orbit: Spectrum of high-energy electrons," *Phys. Rev. D*, vol. 84, p. 013 006, 1 Jul. 2011. DOI: 10.1103/PhysRevD.84.013006. [Online]. Available: https://link.aps.org/doi/10.1103/PhysRevD.84.013006.

[31] S. Huang, "Search for lepton flavor violation in two body muon and pion decay at rest," Ph.D. dissertation, Purdue University, 2022.

[32] T. Kinoshita, "Radiative corrections to $\pi - e$ decay," *Phys. Rev. Lett.*, vol. 2, pp. 477–480, 11 Jun. 1959. DOI: 10.1103/PhysRevLett.2.477. [Online]. Available: https://link.aps.org/doi/10.1103/PhysRevLett.2.477.

[33] M. Bychkov, D. Po ani , B. A. VanDevender, *et al.*, "New precise measurement of the pion weak form factors in $\pi^+ \to e^+ \nu\gamma$ decay," *Phys. Rev. Lett.*, vol. 103, p. 051 802, 5 Jul. 2009. DOI: 10.1103/PhysRevLett.103.051802. [Online]. Available: https://link.aps.org/doi/10.1103/PhysRevLett.103.051802.

[34] M. J. Lamm, N. Andreev, G. Ambrosio, *et al.*, "Solenoid magnet system for the fermilab mu2e experiment," *IEEE Transactions on Applied Superconductivity*, vol. 22, no. 3, pp. 4 100 304–4 100 304, 2012. DOI: 10.1109/TASC.2011.2179835.